The Astrophysical Journal, 818:24 (17pp), 2016 February 10 doi:10.3847/0004-637X/818/1/24

AURORAL RADIO EMISSION FROM LATE L AND T DWARFS: A NEW CONSTRAINT ON DYNAMO THEORY IN THE SUBSTELLAR REGIME

Melodie M. Kao[1], Gregg Hallinan[1], J. Sebastian Pineda[1], Ivanna Escala[2], Adam Burgasser[2], Stephen Bourke[1], and David Stevenson[3]
[1] California Institute of Technology, Department of Astronomy, 1200 E. California Boulevard, MC 249-17, Pasadena, CA 91125, USA; mkao@astro.caltech.edu
[2] University of California San Diego, Center for Astrophysics and Space Sciences, 9500 Gilman Drive, MC 0424, La Jolla, CA 92093, USA
[3] California Institute of Technology, Division of Geological & Planetary Sciences, 1200 E. California Boulevard, MC 150-21, Pasadena, CA 91125, USA
Received 2015 June 25; accepted 2015 November 18; published 2016 February 4

ABSTRACT

We have observed six late L and T dwarfs with the Karl G. Jansky Very Large Array (VLA) to investigate the presence of highly circularly polarized radio emission, associated with large-scale auroral currents. Previous surveys encompassing ∼60 L6 or later targets have yielded only one detection. Our sample includes the previously detected T6.5 dwarf 2MASS 10475385+2124234, as well as five new targets selected for the presence of Hα emission and/or optical infrared photometric variability, which are possible manifestations of auroral activity. We detect 2MASS 10475385+2124234, as well as four of the five targets in our biased sample, including the strong IR-variable source SIMP J01365662+0933473 and bright Hα emitter 2MASS 12373919+6526148, reinforcing the possibility that activity at these disparate wavelengths is related. The radio emission frequency corresponds to a precise determination of the lower-bound magnetic field strength near the surface of each dwarf, and this new sample provides robust constraints on dynamo theory in the low-mass brown dwarf regime. Magnetic fields $\gtrsim$2.5 kG are confirmed for five of six targets. Our results provide tentative evidence that the dynamo operating in this mass regime may be inconsistent with predicted values from a recently proposed model. Further observations at higher radio frequencies are essential for verifying this assertion.

Key words: brown dwarfs – planets and satellites: aurorae – planets and satellites: magnetic fields – radio continuum: stars – stars: individual (SIMP J01365662+0933473) – stars: magnetic field

1. INTRODUCTION

An important outstanding problem in dynamo theory is understanding how magnetic fields are generated and sustained in fully convective stellar objects. Prevailing dynamo models for dwarf stars with an inner radiative zone and an outer convective envelope, like the Sun, are accepted to rely on the shearing at the interface between these two layers, where differential rotation is strongest (Parker 1975). Beyond spectral type ∼M4, stars are fully convective and no longer possess the internal structures necessary to sustain such dynamos (Chabrier & Baraffe 1997). However, flaring M dwarfs are characterized by kilogauss fields covering much of the stellar disk (Saar 1994; Johns-Krull & Valenti 1996), and the fraction of M, L, and T dwarfs that exhibit strong and persistent Hα emission, a magnetic activity tracer, rises through late M dwarfs and peaks at ∼90% for L0 dwarfs before declining to ∼50% for L5 dwarfs (Gizis et al. 2000; West et al. 2004, 2008; Schmidt et al. 2015). Clearly, an alternative dynamo operates in low-mass, fully convective stars. A number of models for possible dynamo mechanisms in this regime have been proposed (Chabrier & Küker 2006; Dobler et al. 2006; Browning 2008; Christensen et al. 2009; Morin et al. 2011b; Gastine et al. 2013), but constraining data on magnetic field strengths and topologies across a wide range of mass, age, rotation, and temperature are sorely lacking, particularly in the brown dwarf regime.

In a recent breakthrough, scaling laws derived from planetary dynamo calculations (Christensen & Aubert 2006) were demonstrated to be empirically consistent with the magnetic field strengths measured for fully convective stars (Christensen et al. 2009; hereafter C09). This result argued for a single unifying principle that governs magnetic activity in rapidly rotating fully convective objects, spanning the mass range from stars to planets—specifically, the energy flux available for generating the magnetic field sets the field strength. This principle states that the magnetic energy in these objects should scale approximately as $\propto\langle\rho\rangle^{1/3}q_0^{2/3}$, where $\langle\rho\rangle$ is the mean density in the dynamo region and q_0 is the bolometric flux. However, while this scaling law appears consistent with magnetic field measurements for solar system planets and fully convective stars, data from the orders-of-magnitude mass gap occupied by rapidly rotating brown dwarfs and massive extrasolar planets are required to validate this principle.

Traditionally, the Zeeman effect has been one of the most powerful means to measure the strength, filling factor, and even large-scale field topology of stellar magnetic fields, including those of fully convective stars. Zeeman broadening of atomic lines such as Fe I has been successfully used to recover the large-scale field topologies of active mid-M dwarfs, confirming that the high levels of coronal and chromospheric activity observed for these stars are indeed associated with strong magnetic fields (typically a few kG) covering a large fraction of the photosphere (with filling factors as high as ∼50%; Johns-Krull & Valenti 1996). Zeeman Doppler imaging (ZDI), involving time-resolved high-resolution spectropolarimetry, has been successfully applied to mid- and late M dwarf stars, both above and below the fully convective boundary (Donati et al. 2006). In some cases strong, large-scale poloidal fields are identified, while in other cases weak, large-scale fields with strong higher-order components are found (Morin et al. 2010), suggesting that a bistable dynamo may operate in the very low mass regime. Probing to even cooler temperatures, Reiners & Basri (2007) were able to use Zeeman broadening of magnetically sensitive molecular lines, such as FeH, to constrain the average surface magnetic fluxes of objects as

late as M9. While these methods have been successful, a robust detection of Zeeman broadening has not been established for objects cooler than late M, as rapid rotational broadening causes blending of the desired molecular lines (Reiners & Basri 2006).

In the past decade, observations of the radio emission from low-mass stars and brown dwarfs have opened a new window on magnetic activity in this regime. While the initial detection of quiescent emission from ∼10% of targets (Berger 2006), possibly consistent with incoherent gyrosynchrotron emission, was itself anomalous (Berger et al. 2001), the later confirmation of a second component to the radio emission, manifested as periodic pulsar-like bursts of 100% circularly polarized emission, was even more unexpected (Hallinan et al. 2006, 2007). This emission is attributed to the electron cyclotron maser (ECM) instability and is of the same nature as the auroral emission produced by the magnetic planets in our solar system via magnetosphere–ionosphere (M–I) coupling. However, unlike the planets, where auroral radio emission is powered by interactions with the solar wind, orbiting satellites, and corotation breakdown, the nature of the electrodynamic engine powering auroral activity in ultracool dwarfs remains unclear (Hallinan et al. 2015).

What is clear is that ECM emission is a very powerful tool for measuring magnetic fields. Produced at the electron cyclotron fundamental frequency $\nu_{\rm MHz} \sim 2.8 \times B_{\rm Gauss}$ (Treumann 2006, and references therein), it allows for very accurate measurements of local magnetic field strengths and rotation periods, and it has provided some of the first confirmations of kilogauss fields for late M and L dwarfs (Burgasser & Putman 2005; Hallinan et al. 2006, 2007, 2008; Berger et al. 2009). Indeed, radio observations have been the only method thus far capable of direct magnetic field measurements for L dwarfs. Examining magnetic dynamo action in the mass gap between planets and stars therefore requires radio data.

Over a dozen low-mass stars and brown dwarfs, ranging in spectral type from M7 to L5, have been found to be radio sources in the past decade (Berger et al. 2001; Berger 2002, 2006; Burgasser & Putman 2005; Antonova et al. 2007; Phan-Bao et al. 2007; McLean et al. 2012; Burgasser et al. 2013, 2015b; Williams et al. 2014). A subset of these objects have been the subject of lengthy follow-up campaigns that have revealed the presence of 100% circularly polarized, periodic pulses, with the pulse period typically 2–3 hr and consistent with rotation (Hallinan et al. 2006, 2007, 2008; Berger et al. 2009). More recently, magnetic field measurements have been extended much further, with the detection of the coolest radio brown dwarf yet detected, the T6.5 dwarf 2MASS J10475385 +2124234 (hereafter 2M1047) by Route & Wolszczan (2012). They observed individual radio pulses from this object in multiple short-duration observations at 4.75 GHz with the Arecibo Observatory, resulting in a confirmed magnetic field strength of at least 1.7 kG near the surface of this extremely cool (∼900 K) object. The results of Route & Wolszczan (2012) highlight the unique capability of radio observations to measure magnetic fields in the critical L and T dwarf regime and show that the latest-type brown dwarfs can in fact host ∼kG field strengths.

However, this single detection came at substantial expense. In previous surveys totaling ∼60 L6 or later type objects, only one was detected (Antonova et al. 2013; Route & Wolszczan 2013), demonstrating that previous selection strategies (largely volume limited) have been inefficient. Motivated by the radio detection of 2M1047, we present a pilot survey of six objects ranging in spectral type from L7.5 to T6.5, including the previously detected T6.5 dwarf 2M1047. We selected our targets using a new strategy, described in Section 2. We measure magnetic field strengths of the coolest brown dwarfs using auroral radio emission, and we study implications on fully convective magnetic dynamo theory.

2. TARGET SELECTION STRATEGY

In a departure from previous surveys, we have selected our objects for tracers of auroral emission at other wavelengths. This selection strategy is motivated by recent work by Hallinan et al. (2015) linking periodic auroral radio emission to Hα emission and optical broadband variability, as well as corroborating evidence that most radio-pulsing ultracool dwarfs exhibit weak Hα emission and/or optical/IR variability.

Hα emission and X-ray emission have been known for decades to scale as power laws of increasing surface rotation or decreasing Rossby number (Ro $\sim P/\tau_c$, where P is the stellar rotation period and τ_c is the convective turnover time) for main sequence F through mid-M stars, until around Ro $\sim$ 0.1, when the activity-rotation scaling appears to saturate at a constant $\log L_{\rm X,H\alpha}/L_{\rm bol}$ (Pallavicini et al. 1981; Soderblom et al. 1993; Stauffer et al. 1994; Delfosse et al. 1998; Pizzolato et al. 2003; Reiners et al. 2009; McLean et al. 2012). Additionally, flaring and quiescent radio emission observed in dwarf stars has been attributed to magnetic activity in the corona (Drake et al. 1989; White et al. 1989), and in fact, X-ray and radio luminosities for magnetically active stars are tightly correlated on the Güdel–Benz relation, spanning 5–6 orders of magnitude and including F through M stars and solar flares (Güdel & Benz 1993). The Güdel–Benz relation holds for active stars independent of age, spectral class, binarity, or rotation period. It suggests that coronal heating and particle acceleration via magnetic fields are related processes (Forbrich et al. 2011, and references therein).

However, beyond $\gtrsim$M7, magnetic activity trends appear to diverge. L and T dwarfs regardless of age appear to be fast rotators (Reiners & Basri 2008), suggesting that they do not spin down with age like M dwarfs. Dwarfs $\gtrsim$M7 also exhibit systematically weaker Hα emission despite being fast rotators, while $L_{\rm X}/L_{\rm bol}$ decreases with increasing $v \sin i$ or decreasing Ro (Mohanty & Basri 2003; Reiners & Basri 2008, 2010; Berger et al. 2010; McLean et al. 2012). In a similar vein, the Güdel–Benz relation appears to break down for objects later than M7 owing to a suppression of X-ray luminosities rather than radio luminosities, even when taking activity-rotation saturation into account (Berger et al. 2010; Williams et al. 2014), suggesting that magnetic activity in L and T dwarfs is no longer dominated by rotation (Cook et al. 2014; Williams et al. 2014). Although radio, Hα, and X-ray luminosities do not necessarily scale with magnetic field strength, their continued emission requires magnetic fields even at very low masses. Zeeman broadening and ZDI studies referenced in Section 1 confirm that ∼kG fields persist in dwarfs as late as M7. In light of such magnetic fields, a simple explanation for the observed activity breakdowns may be the decoupling of magnetic fields from increasingly neutral atmospheres (Mohanty et al. 2002).

However, clearly nonthermal heating of the upper atmospheres of ultracool dwarfs is commonplace and sustained. The breakdown of activity trends in late-type dwarfs indicates that

the persistence of Hα, X-ray, and radio emission perhaps reflects a departure from the standard chromospheric heating picture where magnetic fields locally interact with hotter and less neutral atmospheres. Instead, activity may be externally powered via auroral current systems such as M–I coupling currents, giving rise to auroral activity (Schrijver et al. 2011; Nichols et al. 2012; Hallinan et al. 2015). M–I coupling has been confirmed as a source of power for Jovian, Saturnian, and terrestrial auroral emissions (Hill 1979; Nichols et al. 2012; Bagenal et al. 2014; Badman et al. 2015, and references therein).

Recently, Hallinan et al. (2015) have established that radio emission may only be one manifestation of auroral activity, as is observed for the planets in our solar system. These authors have shown that the M8.5 dwarf LSR J1835+3259 is simultaneously variable with the same periodicity in broadband optical, Balmer line, and pulsed radio emission. The radio and Hα luminosities, together with the synchronized variability, are consistent with the emission in all bands being powered by the same auroral currents. Hallinan et al. (2015) also postulated that there may be a causal relationship between auroral currents and some examples of the infrared variability (weather) observed for L and T dwarfs, though they presented no empirical data to support this hypothesis.

Such synchronized multiwavelength emission has been previously observed in other radio brown dwarfs. TVLM 513–46546 (M8.5) exhibited anticorrelated Sloan-g' and Sloan-i' light curves, which Littlefair et al. (2008) attributed to cloud phenomena, and Hα emission from 2MASSW J0746425+200032 (L0+L1.5) was variable with the same periodicity as its pulsed radio emission but at a 1/4-phase lag (Berger et al. 2009). In fact, all but one of the known radio-pulsing ultracool dwarfs also exhibit Hα emission, and several are also confirmed optical/IR variables (Tinney & Reid 1998; Basri 2001; Delfosse et al. 2001; Hall 2002; Reid et al. 2002; Mohanty & Basri 2003; Fuhrmeister & Schmitt 2004; Lane et al. 2007; Schmidt et al. 2007; Littlefair et al. 2008; Berger et al. 2009, 2010; Reiners & Basri 2010; Antonova et al. 2013; Harding et al. 2013; Burgasser et al. 2015a, and references therein).

Motivated by the above discussion, we strongly bias our samples for auroral activity by targeting only those dwarfs in this spectral range known to exhibit Hα emission and/or optical/IR variability.

3. TARGETS

2MASS 10475385+2124234. Discovered by Burgasser et al. (1999), 2M1047 was later classified as a T6.5 brown dwarf by Burgasser et al. (2006b). Burgasser et al. (2003) detected weak Hα emission at the 2.2σ level with a flux of $f_{\rm H\alpha} = (5.9 \pm 2.7) \times 10^{-18}$ erg cm^{-2} s^{-1}. In 2012, 2M1047 became the first T dwarf detected in the radio, when Route & Wolszczan (2012) detected highly circularly polarized ($\gtrsim$72%) and bright flares at 4.75 GHz with ∼1.3–2.7 mJy peak flux densities using the Arecibo telescope. Until this study, it has remained the only radio-detected ⩾L6 dwarf. A follow-up study by Williams et al. (2013) at 5.8 GHz using the Very Large Array (VLA) found quasi-quiescent radio emission from this source with a flux density of 16.5 ± 5.1 μJy. Williams & Berger (2015) confirmed quiescent emission for 2M1047, measuring flux densities of 9.3 ± 1.5 and 1.1 ± 1.5 μJy at 6–10 GHz for Stokes I and V, respectively, with low circular polarization ($\lesssim$28%). They also detected highly left circularly polarized pulses (∼50%–100%) with a periodicity of ∼1.77 hr up through 10 GHz. We include 2M1047 in our survey as a known quiescently emitting source and to examine long-term variability.

SIMP J01365662+0933473. SIMP0136 was discovered and classified as a T2.5 dwarf by Artigau et al. (2006). In a follow-up study, Artigau et al. (2009) reported J- and K_s-band photometric variability, with a peak-to-peak amplitude $\Delta J \sim 50$ mmag, an amplitude ratio $\Delta K_s/\Delta J = 0.48 \pm 0.06$, and a period $P = 2.3895 \pm 0.0005$ hr. This was the first clearly periodic and high-amplitude detection of IR variability in a T dwarf. They attributed the variability to clouds that are ∼100 K colder than a surrounding cloud-free atmosphere in the brown dwarf. Using *Hubble Space Telescope* (*HST*) spectral mapping, Apai et al. (2013) found that models of low-temperature and thick clouds mixed with warmer and thin clouds can reproduce time-variable changes in the near-IR colors and spectra of SIMP0136, and they confirmed that it had a stable variation period.

2MASS 10430758+2225236. 2M1043 was discovered and classified as an unusually red L8 dwarf by Cruz et al. (2007), which they speculated could be attributed to an unresolved binary. A follow-up study by Reid et al. (2008) using the NICMOS N1C1 camera on the *HST* found that no binary companion to 2M1043 was resolved, for mass ratios $q > 0.2$ and angular separations $\theta > 0\farcs3$. In the discovery paper, the authors also tentatively report possible Hα emission.

2MASS 12373919+6526148. 2M1237 was discovered by Burgasser et al. (1999) using data from the Two Micron All Sky Survey (2MASS; Skrutskie et al. 2006) and classified as a T6.5 dwarf by Burgasser et al. (2002b). Burgasser et al. (2000b, 2002b) reported abnormally bright and persistent yet variable Hα emission, which was confirmed again by Burgasser et al. (2003). With fluxes in the range $f_{\rm H\alpha} \sim (1\text{–}10) \times 10^{-17}$ erg cm^{-2} s^{-1}, the Hα luminosity is an order of magnitude higher than for any other T dwarf. Burgasser et al. (2002b) found no evidence of short-term J-band variability and ruled out flaring as a possible variability mechanism. In contrast, Artigau et al. (2003) reported variability at $\Delta J \sim 30$ mmag. Liebert & Burgasser (2007) ruled out a massive companion or youthful chromospheric activity as additional possible Hα variability mechanisms.

SDSS J12545393–0122474. SDSS1254 was discovered by Leggett et al. (2000) and independently classified as a T2 dwarf by both Burgasser et al. (2002a) and Geballe et al. (2002) and is the T2 spectral standard (Burgasser et al. 2006b). Burgasser et al. (2003) reported weak Hα emission with flux $f_{\rm H\alpha} = (7.5 \pm 2.5) \times 10^{-18}$ erg cm^{-2} s^{-1}. Artigau et al. (2003) reported 45 ± 2 mmag J-band and 23 ± 4 mmag H-band variability, and similarly, Goldman et al. (2008) reported variable spectral features at 0.997–1.13 μm, with upper limits in the peak-to-peak flux variability calculated at the ∼4%–60% levels. In contrast, Koen et al. (2004) found no evidence of variability above the 7, 6, and 10 mmag levels for J, H, and K_s bands during a ∼4-hr observation, and Girardin et al. (2013) found no evidence of J-band variability above 5 mmag. We note here that SDSS1254 appears to be sufficiently overluminous for its spectral type that it may in fact be an as-yet-unresolved tight binary system (Burgasser 2007; Cushing et al. 2008).

Table 1
Survey Targets

Object Name	Abbrev. Name	SpT	Parallax (mas)	Distance (pc)	$\mu_\alpha \cos\delta$ (mas yr^{-1})	μ_δ (mas yr^{-1})	Notes	Ref.
2MASS 10475385 +2124234	2M1047	T6.5	94.73 ± 3.81	10.56 ± 0.52	−1714 ± 7	−489 ± 4	Hα, detected prior	(1)–(7)
2MASS 01365662 +0933473	SIMP0136	T2.5	…	6.0 ± 0.4	1241 ± 9	−4 ± 10	IR variability	(8)–(10)
2MASS 10430758 +2225236	2M1043	L8	…	16.4 ± 3.2	−134.7 ± 11.6	−5.7 ± 17.0	Hα emission	(11)–(13)
2MASS 12373919 +6526148	2M1237	T6.5	96.07 ± 4.78	10.42 ± 0.52	−1002 ± 8	−525 ± 6	Hα, IR var?[a]	(1), (3), (4), (14)–(16)
SDSS J12545393–0122474	SDSS1254	T2	75.71 ± 2.88	13.21 ± 0.50	−479 ± 3	130 ± 2	Hα, IR var?[b], binary?[c]	(17), (3), (4), (18)–(26)
SDSS 04234858–0414035	SDSS0423	L7[d]	65.93 ± 1.7	15.17 ± 0.39	−331 ± 49	76 ± 11	Hα, IR var, binary[d]	(19), (27)–(33)

Notes.
[a] (14) found no evidence of *J*-band variability, whereas (16) reported variability at a level below the detection limits of (14).
[b] (22)–(24) found no IR variability in SDSS1254 above the ∼5–20 mmag level, whereas (20) and (21) reported significant *J*-band and spectroscopic variability, respectively.
[c] See (25), (26), and Sections 6.2 and 3 for further discussion about possible multiplicity in SDSS1254.
[d] SDSS0423 has a known binary companion of spectral type T2.5 and orbital separation 0.″16 ((31), (32), (33)).
References. (1) Burgasser et al. 1999; (2) Burgasser et al. 2006b; (3) Vrba et al. 2004; (4) Burgasser et al. 2003; (5) Route & Wolszczan 2012; (6) Williams et al. 2013; (7) Williams & Berger 2015; (8) Artigau et al. 2006; (9) Artigau et al. 2009; (10) Apai et al. 2013; (11) Cruz et al. 2007; (12) Schmidt et al. 2010; (13) Pineda et al. (submitted to ApJ); (14) Burgasser et al. 2002b; (15) Burgasser et al. 2000b; (16) Artigau et al. 2003; (17) Leggett et al. 2000; (18) Burgasser et al. 2002a; (19) Geballe et al. 2002; (20) Artigau et al. 2003; (21) Goldman et al. 2008; (22) Koen et al. 2004; (23) Girardin et al. 2013; (24) Radigan et al. 2014; (25) Burgasser 2007; (26) Cushing et al. 2008; (27) Cruz et al. 2003; (28) Kirkpatrick et al. 2008; (29) Enoch et al. 2003; (30) Clarke et al. 2008; (31) Carson et al. 2011; (32) Burgasser et al. 2005; (33) Burgasser et al. 2006a.

SDSS 04234858–0414035. SDSS0423 was identified by Geballe et al. (2002) using data from the Sloan Digital Sky Survey (York et al. 2000). The authors classified it as a T0 dwarf on the basis of its infrared spectrum. However, using its optical spectrum, Cruz et al. (2003) classified it as an L7.5. Burgasser et al. (2005) showed that it is in fact a binary system of two brown dwarfs with spectral types L6 ± 1 and T2 ± 1, consistent with the previous classifications. Both Burgasser et al. (2005) and Carson et al. (2011) reported the angular separation of the binary to be 0.″16, which we cannot resolve with our observations. For the purposes of comparing our magnetic field measurements with previous models, we adopt a conservative L7.5 classification. Monitoring in K_s band by Enoch et al. (2003) yielded only a possible detection of variability, whereas Clarke et al. (2008) reported *J*-band photometric variability with a peak-to-peak amplitude of 8.0 ± 0.8 mmag and a period of 2 ± 0.4 hr. SDSS0423 is additionally one of only a handful of late L/T dwarfs to exhibit Hα emission, for which Kirkpatrick et al. (2008) reported an equivalent width of 3 Å.

4. OBSERVATIONS

We observed six objects spanning spectral range L7.5–T6.5 with the full VLA array in *C* band (4–8 GHz), using the WIDAR correlator in 3-bit observing mode for 4 GHz bandwidth observations, in time blocks of 2 or 4 hr for 28 total program hours. Observations were performed between 2013 March and August, during DnC and C configurations. We summarize target properties and observations in Tables 1 and 2, respectively.

4.1. Calibrations

We calibrated our measurement sets using standard VLA flux calibrators 3C 286 and 3C 147 and nearby phase calibrators. After initially processing raw measurement sets with the VLA Calibration Pipeline, we manually flagged remaining RFI. Typical full-bandwidth sensitivity at DnC configuration for 2 hr on source in *C* band is 3 μJy. Typical 3-bit observations reach an absolute flux calibration accuracy of ∼5%. We obtained absolute flux by bootstrapping flux densities with standard VLA flux calibrators. Flux calibration accuracy may be reduced and result in systematically offset flux densities when gain calibrations interpolated from the phase calibrator are not sufficient to correct for the variation of gain phases with time. To account for this, our observations alternated between a nearby phase calibrator and the target source with typical cycle times of 30 minutes, and we obtained gain solutions for the phase calibrators that varied slowly and smoothly over time, suggesting that this source of error is negligible.

4.2. Source Motion

The expected positions of the sources were determined using 2MASS coordinates (Skrutskie et al. 2006) and corrected for proper motion, provided in Table 1. Sources had moved by as much as 0.″8 owing to proper motion during our observing program, in comparison to synthesized beam resolutions of at least a few arcseconds. Orbital motion corrections were not necessary for SDSS0423, a known binary with an orbital separation of 0.″16. We compared the expected coordinates of our objects with their measured position and found that all

Table 2
Summary of Observations

Object	Band (GHz)	Obs. Date (2013)	Obs. Block (h)	Time on Source (s)	VLA Configuration	Synthesized Beam Dimensions (arcsec×arcsec)	rms (μJy)	Phase Calibrator	Flux Calibrator
2M1047	4.0–8.0	05/19	4.0	12745	DnC	9.21 × 3.02	3.1	J1051+2119	3C 286
SIMP0136	4.0–8.0	05/18	4.0	12995	DnC	8.64 × 3.10	5.4	J0203+1134	3C 147
2M1043	4.0–8.0	05/25	4.0	13042.5	DnC	10.0 × 5.5	2.0	J1051+2119	3C 286
	4.0–8.0	05/27	2.0	5825	DnC	9.82 × 5.47	4.9	J1051+2119	3C 286
2M1237	4.0–8.0	05/21	2.0	5712.5	DnC	8.22 × 3.70	2.8	J1313+6735	3C 286
SDSS1254 [a]	4.0–8.0	05/19	2.0	5685	DnC	9.70 × 3.55	4.0	J1246–0730	3C 286
	4.0–8.0	05/26	2.0	⋯	DnC	⋯	⋯	J1246–0730	3C 286
SDSS0423	4.0–8.0	08/30	4.0	13102.5	C	4.91 × 3.37	3.2	J0423–0120	3C 147
	4.0–8.0	05/26	2.0	5907.5	DnC	11.52 × 5.96	4.0	J0423–0120	3C 147
	4.0–8.0	05/25	2.0	5925	DnC	12.92 × 9.11	3.5	J0423–0120	3C 147

Note.
[a] Excessive noise prevented successful calibration of the measurement set taken on 2013 May 23.

objects were well within a synthesized beam of their predicted locations.

5. RESULTS

5.1. Image Detections

We combined measurement sets for objects with multiple observing blocks using the CASA `concat` routine and then produced Stokes *I* and Stokes *V* images of each object (total and circularly polarized intensities, respectively) with the CASA `clean` routine, modeling the sky emission frequency dependence with two terms and using Brigg's weighting with the robustness parameter set to 0.0, which we found resulted in a good trade-off between resolution and sensitivity for our observations. We searched for a point source at the proper-motion-corrected coordinates of each target. Figure 1 shows the Stokes *I* and Stokes *V* images for all objects.

In contrast to previous surveys, all but one of our six targets were detected in Stokes *I*, with signal-to-noise ratios (S/Ns) ranging from 4.9 to 24.6 in the mean Stokes *I* flux density. Table 3 gives the measured mean flux density and rms noise of each detected (S/N $\geqslant$ 3) source. Flux densities and source positions were determined by fitting an elliptical Gaussian point source to the cleaned image of each object at its predicted coordinates, using the CASA task `imfit`. For the one undetected target, SDSS1254, we provide the measured mean Stokes *I* flux density and rms noise at the expected position of the source.

5.2. Time Series Pulse Detections and Magnetic Field Strengths

We checked all targets for highly circularly polarized pulses in flux density to confirm the presence of ECM emission. Previous studies have searched for pulsed emission in Stokes *I* and *V*, but we have chosen to search for pulses in the rr and ll correlations (right and left circularly polarized, respectively) because S/N is a factor of $\sqrt{2}$ higher in cases where the pulsed emission is 100% circularly polarized.

Using the CASA plotting routine `plotms` to export the real UV visibilities averaged across all baselines, channels, and spectral windows of the rr and ll correlations, we created rr and ll time series for all measurement sets with time resolutions of 10, 60, and 600 s at frequency ranges of 4–6, 6–8, and 4–8 GHz to check for frequency-dependent ECM emission cutoff. We do not check for pulses at frequency resolutions smaller than 2 GHz owing to S/N concerns. Figure 2 shows the 4–8 GHz time series for each object.

Analysis of the time series shows significant evidence of at least one pulse for 2M1047, SIMP0136, SDSS0423, and 2M1043. Additionally, 2M1237 appears to exhibit very broad pulses or strongly variable emission. We confirm pulses by imaging right circularly polarized and/or left circularly polarized emission over the FWHM of each pulse and measuring integrated flux densities using the CASA routine `imfit` at the expected locations of our targets. We find that flux densities for imaged pulses are consistent with pulses observed in the time series within 3σ. For all objects except for 2M1237, we smooth our data over 60, 90, and 180 s to measure the FWHM. We find that the FWHM is consistent within ∼30 s, except for the earlier ll pulse on 2013 August 30 for SDSS0423; when the smoothing is extended to 180 s, the narrow peak smears out into the broader bump, and the returned FWHM is accordingly broader. For the purposes of measuring a mean pulsed flux, we use the narrower FWHM. Because of the broad nature of the peaks for 2M1237, we smooth over 180, 270, and 540 s and find that the FWHM is consistent within ∼450 s.

We measure the mean pulsed Stokes *I* and *V* flux densities by imaging over all of the pulses with peak flux density $\geqslant$3.0 for each object and calculate the highest-likelihood percent circular polarization of the mean pulsed flux, where negative and positive percentages correspond to left and right circular polarization, respectively. We report uncertainties that correspond to the upper and lower limits of the 68.27% confidence interval. We find that in all cases except for the first peak in 2M1237, the pulsed emission is highly circularly polarized (48.8%–97.3%), consistent with ECM emission (Treumann 2006).

We additionally check for quiescent emission by removing the full width of each pulse from our data and imaging the remaining emission. We define the full width of the pulse as beginning and ending at the time bins nearest the pulse maximum that have flux densities less than or equal to the rms noise. We find that pulse widths for each object are consistent within ∼60 s (∼500 s for 2M1237) for all smoothing resolutions, and we select the widest returned width when removing

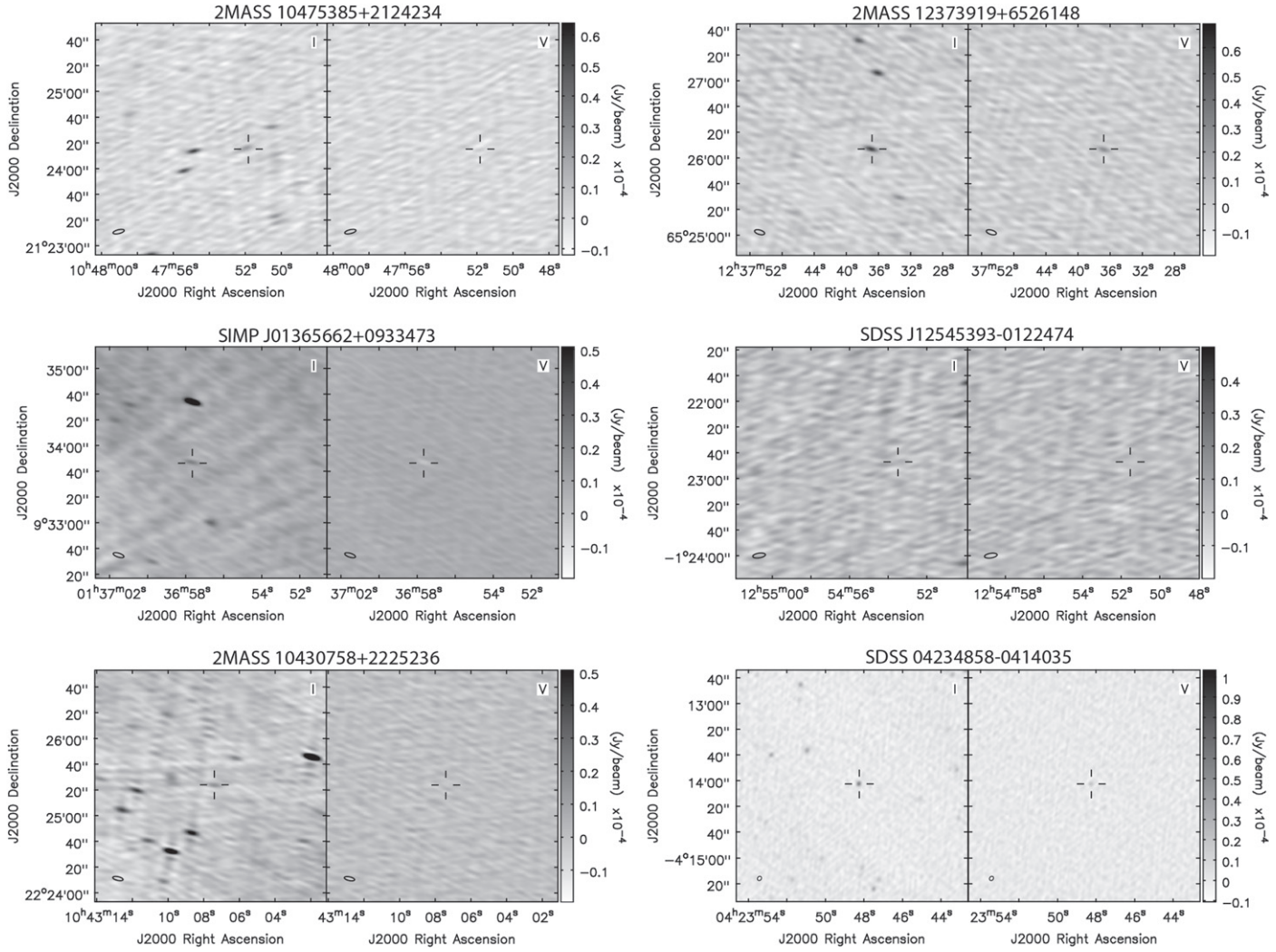

Figure 1. Stokes *I* (left) and *V* (right) images of all objects. Ellipse depicts synthesized beam. Measurement sets for objects with multiple observing blocks were concatenated prior to imaging. Sources were detected at the proper-motion-corrected location for all objects except for SDSS1254.

each pulse. All objects with pulsed emission also exhibit quiescent emission with relatively low polarization fractions, except for 2M1237. In contrast, SDSS1254, for which no pulse is observed, does not exhibit any detectable quiescent emission above the rms noise. We report the characteristics of the pulsed and quiescent emission in Table 3 and show their stokes *I* and *V* images in Figure 3.

Searching for the FWHM of 2M1047 reveals an apparent double peak, similar to what Williams & Berger (2015) observe. Based on the periodicity observed by Williams & Berger (2015), we classify this object as having a single pulse. However, in measuring the mean pulsed flux densities, we treat it as a double pulse and average over the FWHM of each pulse.

Two extremely bright sources near SIMP0136 resulted in poor Stokes *I* field source subtraction, and our reported Stokes *I* flux density is certainly an underestimate of the true flux density. We attempted to self-calibrate this field but were only able to achieve ∼10% improvement. Beam squint causes the nearby bright sources to also appear in Stokes *V* but with much lower flux densities, and we therefore consider the Stokes *V* flux density of SIMP0136 to be more accurate. Because the degree of circular polarization cannot be greater than 100%, the Stokes *V* flux density in fact gives a lower bound on the actual Stokes *I* flux density. From its extremely bright Stokes *V* flux density, we conclude that pulses from SIMP0136 are highly circularly polarized.

We note that our observations only tentatively suggest that we observe ECM emission from 2M1237. Despite the broad nature of the peaks in 2M1237, it is possible that the time series in fact exhibits two pulses rather than simply being variable, with the broadness arising from a geometric effect. We report the flux densities and circular polarization fractions for each of the peaks in the 2M1237 rr time series, and we find that in fact the circular polarization fraction appears to vary from peak to peak, from ∼30% to ∼50% on a 2 hr timescale. Some of the variability may arise from the incomplete phase coverage, such that the earlier peak is averaged down more than the later peak. Whereas the other radio-detected objects all exhibit marked differences in polarization fractions between pulsed and quiescent emission, the "quiescent" emission from 2M1237 exhibits ∼50% circular polarization, which is similar to what we observe in at least one of the peaks. This could be consistent with a geometry in which the ECM-emitting region of the magnetosphere is always visible, which would also explain the broadness of the peaks. Additional monitoring of 2M1237 for

Table 3
Imaging and Time Series Results

Object	Position Offset [a] (sigma)	Mean Stokes I (μJy)	Pulse #	Pulse Stokes I (μJy)	Pulse Stokes V (μJy)	S/N (I, V)	Pulse Circ. Poln (%)[b]	Quiescent Stokes I (μJy)	S/N	Quiescent Circ. Poln (%)[b]
2M1047	1.46	26.8 ± 3.1	1	123.0 ± 21.0	-95.0 ± 15.0	5.9, 6.3	$-75.1^{+14.1}_{-14.9}$	17.5 ± 3.6	4.9	$-40.6^{+23.4}_{-13.2}$
SIMP0136	0.36	34.4 ± 5.4	2	$>156.0 \pm 39.7$ [c]	-233.0 ± 24.9	3.9, 9.4	-63.6 [d]	33.3 ± 5.9	5.6	-1.2 [d]
2M1043	0.79	11.7 ± 2.4	3	87.0 ± 11.8	-69.0 ± 11.7	7.4, 5.9	$-77.9^{+15.1}_{-13.0}$	16.3 ± 2.5	6.5	$-13.8^{+13.8}_{-15.9}$
2M1237 [e]	2.91	64.7 ± 3.7	2? [f]	83.3 ± 7.6	23.7 ± 6.4	9.5, 3.7	$28.2^{+9.0}_{-7.5}$	43.3 ± 7.3	5.9	$53.7^{+21.6}_{-14.6}$
	…	…	…	81.7 ± 8.8	40.3 ± 8.0	9.3, 5.0	$48.8^{+13.1}_{-9.7}$	…	…	…
SDSS1254	…	3.3 ± 4.0	0	…	…	…	…	…	…	…
SDSS0423 [g]	0.42	54.1 ± 2.2	10	225.4 ± 12.4	220.0 ± 12.2	18.2, 18.0	$97.3^{+0.8}_{-9.0}$	26.7 ± 3.1	8.6	$14.4^{+11.5}_{-10.2}$
	…	…	…	135.0 ± 9.8	-67.1 ± 7.9	13.8, 8.5	$-49.4^{+6.1}_{-7.8}$	…	…	…

Notes.
[a] The distance between the measured and expected coordinates, divided by the amplitude of the error ellipse in the offset direction, using concatenated images for objects with multiple observing blocks. 2MASS coordinate uncertainties and our own measurement uncertainties were included in error analysis.
[b] Reported polarization fractions are highest-likelihood values, given the measured Stokes I and Stokes V flux densities. Uncertainties reflect the upper and lower bounds of the 68.27% confidence intervals. Negative values indicate left circular polarization, and positive values indicate right circular polarization.
[c] Challenges with field source subtraction result in an underestimate of the true Stokes I flux density. Because circular polarization cannot exceed 100%, the Stokes V flux density gives a lower bound to the true Stokes I flux density.
[d] We quote the lower bound of the 99.73% confidence interval for the percent circular polarization of SIMP0136 owing to an underestimated Stokes I flux density.
[e] Owing to the broadness of the two observed peaks in the rr time series of 2M1237, we report measurements separately for each peak. The top measurement is for the earlier peak, and the bottom measurement is for the later peak.
[f] See Section 5.2 for discussion.
[g] We observe two sets of pulses, six in the rr time series (top) and four in the ll time series (bottom).

full phase coverage is necessary to determine the nature of these peaks.

Three possibilities may account for why we do not observe a pulse from SDSS1254: (1) SDSS1254 does not produce ECM emission, (2) SDSS1254 produces ECM emission with a cutoff frequency lower than 4.0 GHz, or (3) we did not observe it during a pulse and the auroral activity is variable. Table 3 summarizes time series data for all objects. All detected pulses extend into the 6.0–8.0 GHz band, indicating that observations at higher frequencies are required to detect and measure an emission cutoff. We conservatively use the center of the top band, 7.0 GHz, to calculate corresponding lower-bound maximum surface field strengths of 2.5 kG.

6. DISCUSSION

6.1. Auroral Radio Emission as a Precise Tool for Magnetic Field Measurement

Auroral ECM emission from the planets in our solar system is produced very close to the fundamental electron cyclotron frequency local to the source region. Though intrinsically narrowband ($\Delta\nu \ll \nu$), the emission can be detected over a wide range of frequencies, as the process operates efficiently over a range of heights above the planetary surface, which maps to a range of field strengths. Taking the Jovian case as an example, auroral radio emission is detected from 10 KHz to 40 MHz frequencies, with the lowest-frequency emission originating in source regions out to $>5\ R_J$, and the high-frequency emission corresponding to the highest-strength magnetic field regions (14 G) just above the atmosphere in the auroral polar regions in the northern hemisphere (Zarka 1998). Observed remotely, independent of knowledge of the source region or the electrodynamic engine powering the auroral currents, the high-frequency cutoff of this emission provides a good means to determine the maximum magnetic field strength in the magnetospheres of the magnetized planets.

We propose to utilize the highly circularly polarized component of the radio emission detected from our sample of cool brown dwarfs to similarly constrain the maximum magnetic field strengths in their magnetospheres, with a view to constraining the dynamo mechanism at work in their interiors. In the absence of a clear cutoff in emission, we note that any detection can be equated to a robust lower limit on a maximum surface magnetic field strength. While the detection of such ECM emission provides exquisite measurement of local magnetic field strengths at the source of the radio emission, this must be translated to global parameters of particular use to dynamo modeling. Similarly, care must be taken in comparing these measurements with magnetic field measurements previously obtained for higher-mass objects via Zeeman splitting/broadening and ZDI, as they are measuring distinct but complementary properties of the magnetic field. We address these issues in Section 6.3.

The ECM emission from our sample is detected across the entire band of our observations, which spans 4–8 GHz. Thus, in the absence of a clear cutoff in the emission, we can place a lower limit to the maximum surface magnetic field strength of 2.5 kG for all of our detected sample. This assumes that the emission is produced at the fundamental electron cyclotron frequency, rather than a higher harmonic, as is the case for solar system planets. ECM emission at higher harmonics has been invoked to explain coherent radio bursts from the Sun and active stars, where the coronal density is such that second-harmonic cyclotron absorption may prevent escape of emission at the fundamental frequency. Indeed, it has been shown that emission at the second and higher harmonics can dominate when the ratio of the plasma frequency to the electron cyclotron frequency exceeds ~0.3 (Winglee 1985). However, in the case of our sample, this would require a local plasma density of $\sim 10^{11}\ \mathrm{cm}^{-3}$, more indicative of hot stellar coronae than the cool neutral atmospheres of late L and T dwarfs, motivating the

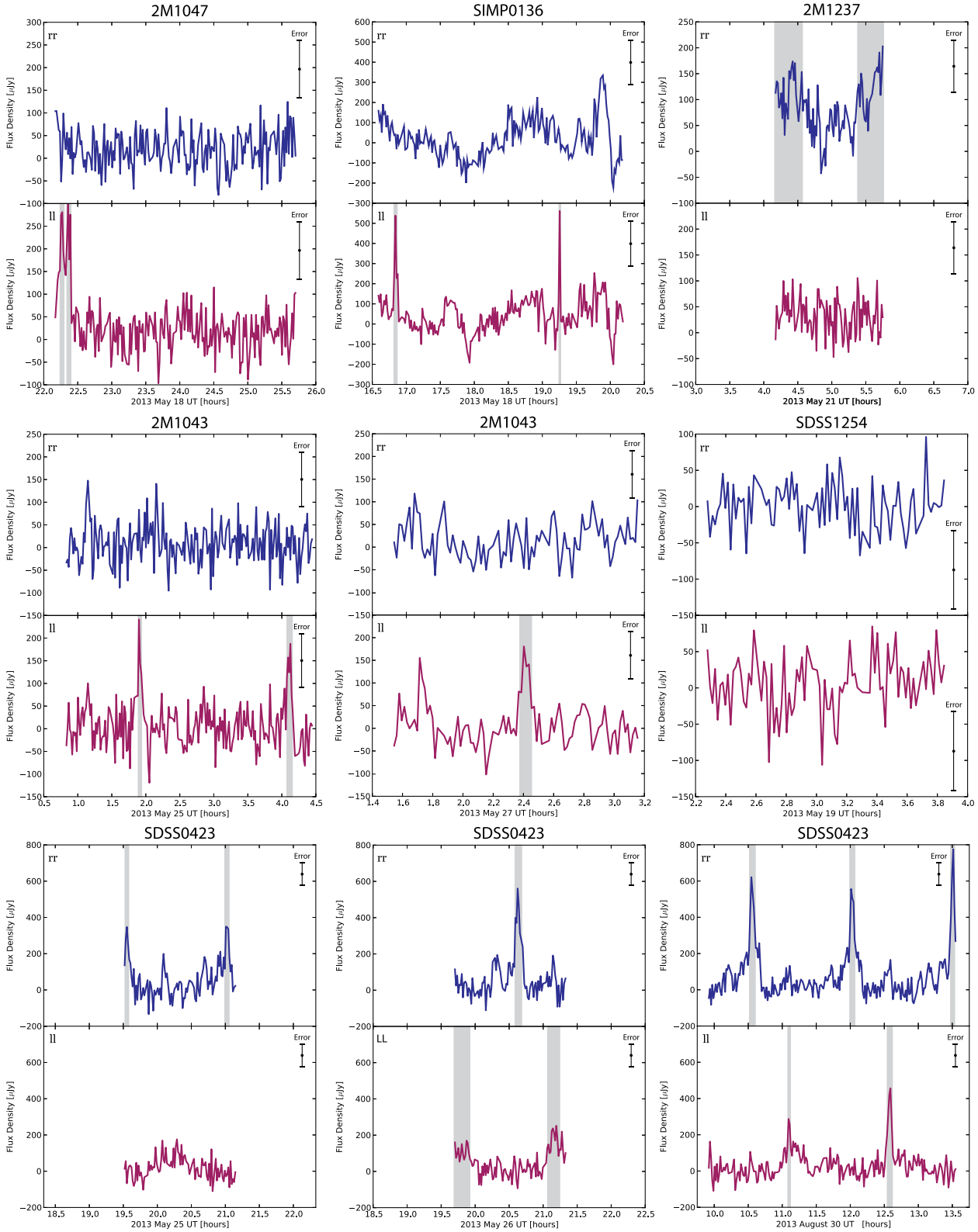

Figure 2. Time series of rr- and ll-correlated (blue for right circularly polarized and red for left circularly polarized, respectively) flux densities for all calibrated measurement sets. Axis scales are constant for time series for objects with multiple observing blocks. For presentational clarity, data are averaged over 60 s intervals; time interval for raw data was 5 s, and all analysis was done with data averaged over 10 s. Black error bars represent rms noise obtained in images and scaled to time bin lengths for a single correlation. Gray regions indicate FWHM of pulses with peak flux density $\geqslant$3.0, and all pulses have been verified with imaging. Total intensity is given by the Stokes I flux density, where $I = (\mathrm{rr}+\mathrm{ll})/2$. Circularly polarized intensity is given by the Stokes V flux density, where $V = (\mathrm{rr}-\mathrm{ll})/2$.

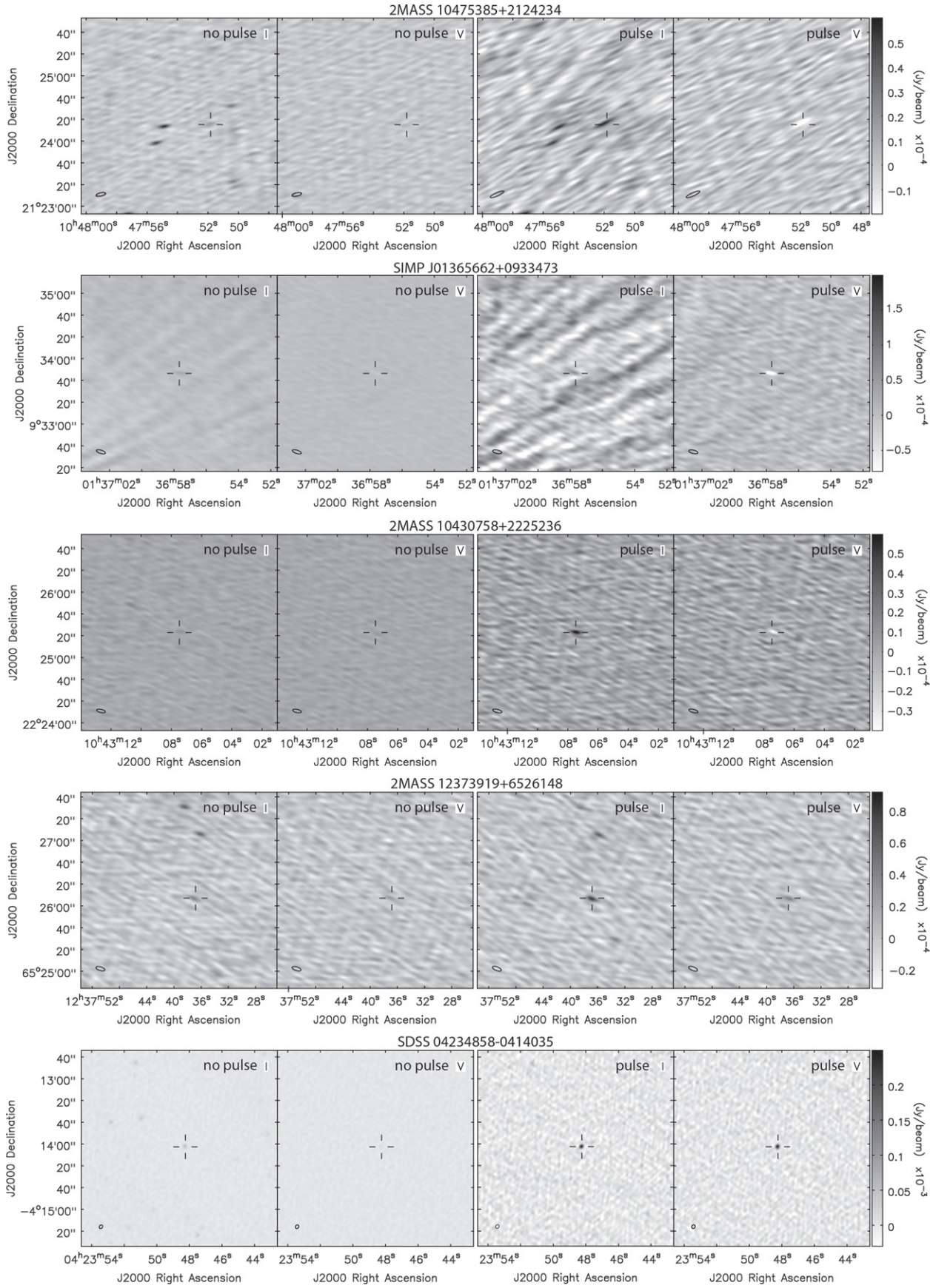

Figure 3. Stokes *I* and Stokes *V* flux densities for pulsed and quiescent emission. Pulsed emission for 2M1237 is averaged only over the later pulse, and SDSS0423 pulsed emission is averaged over the rr pulses only.

Table 4
Brown Dwarf Physical Parameters

Object	SpT	$T_{\rm eff}$ [a] (K)	log g [a] (cm s^{-2})	Age [b] (Gyr)	Mass [b] ($M_\odot$)	Adopted $T_{\rm eff}$ [c] (K)	Adopted log g [c] (cm s^{-2})	Adopted Age [c] (Gyr)	Adopted Mass [c] ($M_\odot$)
2M1047	T6.5	888^{+33}_{-33}	$5.34^{+0.11}_{-0.46}$	>2.5	>0.026	869^{+35}_{-29}	$5.29^{+0.10}_{-0.28}$	>2.5	>0.026
		850^{+62}_{-47}	$5.23^{+0.18}_{-0.25}$	>2.5	>0.026	...	...	...	...
SIMP0136	T2.5	1104^{+51}_{-63}	$4.78^{+0.35}_{-0.40}$	$0.6^{+1.1}_{-0.3}$	$0.022^{+0.015}_{-0.012}$	1089^{+62}_{-54}	$4.79^{+0.26}_{-0.33}$	$0.6^{+1.1}_{-0.3}$	$0.022^{+0.015}_{-0.012}$
		1073^{+112}_{-87}	$4.79^{+0.39}_{-0.52}$	$0.7^{+1.1}_{-0.3}$	$0.022^{+0.015}_{-0.012}$	...	...	...	...
2M1043 [d]	L8	1012^{+64}_{-90}	$3.94^{+0.13}_{-0.09}$	$0.6^{+3.4}_{-0.3}$	$0.011^{+0.011}_{-0.005}$	1390 ± 180	...	$0.6^{+4.6}_{-0.3}$	$0.011^{+0.011}_{-0.005}$
		1229^{+212}_{-260}	$4.28^{+0.49}_{-0.34}$	$0.6^{+4.6}_{-0.3}$	$0.011^{+0.011}_{-0.005}$	...	...	...	...
2M1237	T6.5	851^{+36}_{-32}	$5.39^{+0.08}_{-0.26}$	>3.4	>0.028	831^{+31}_{-27}	$5.34^{+0.08}_{-0.17}$	>3.4	>0.028
		810^{+51}_{-43}	$5.28^{+0.15}_{-0.21}$	>3.4	>0.028	...	...	...	...
SDSS1254	T2	1079^{+56}_{-63}	$4.52^{+0.41}_{-0.35}$	$0.49^{+0.51}_{-0.21}$	$0.017^{+0.015}_{-0.008}$	1070^{+69}_{-52}	$4.57^{+0.30}_{-0.27}$	$0.49^{+0.51}_{-0.21}$	$0.017^{+0.015}_{-0.008}$
		1061^{+127}_{-83}	$4.62^{+0.43}_{-0.40}$	$0.49^{+0.48}_{-0.21}$	$0.017^{+0.015}_{-0.008}$	...	...	...	...
SDSS0423 [e]	L7+T2.5	1084^{+71}_{-41}	$4.25^{+0.34}_{-0.18}$	$0.42^{+0.62}_{-0.17}$	$0.015^{+0.021}_{-0.006}$	1678^{+174}_{-137}	...	$0.43^{+0.62}_{-0.17}$	$0.015^{+0.021}_{-0.006}$
		1150^{+198}_{-114}	$4.50^{+0.57}_{-0.35}$	$0.43^{+0.61}_{-0.17}$	$0.014^{+0.020}_{-0.006}$	...	...	...	...
Gl 570D	T7.5	817^{+32}_{-36}	$5.02^{+0.19}_{-0.48}$	$2.4^{+1.6}_{-1.7}$	$0.024^{+0.011}_{-0.010}$	799^{+40}_{-32}	$4.96^{+0.18}_{-0.32}$	$2.4^{+1.6}_{-1.7}$	$0.024^{+0.011}_{-0.010}$
		781^{+73}_{-53}	$4.90^{+0.32}_{-0.37}$	$2.4^{+1.6}_{-1.7}$	$0.024^{+0.011}_{-0.010}$	...	...	...	...
HN Peg B	T2.5	1054^{+51}_{-66}	$4.60^{+0.37}_{-0.44}$	$0.6^{+0.6}_{-0.3}$	$0.018^{+0.016}_{-0.009}$	1043^{+59}_{-51}	$4.64^{+0.28}_{-0.32}$	$0.6^{+0.6}_{-0.3}$	$0.018^{+0.017}_{-0.009}$
		1032^{+107}_{-77}	$4.67^{+0.40}_{-0.45}$	$0.6^{+0.6}_{-0.2}$	$0.017^{+0.015}_{-0.009}$	...	...	...	...

Notes.
[a] (Top) cf. Gl 570D, (bottom) see HN Peg B. Calibrators Gliese 570D and HN Peg B included for reference. Minus and plus errors define the 68.27% confidence interval.
[b] Mass and age estimates from evolutionary models of Baraffe et al. (2003), using input parameters determined from (top) cf. Gl 570D and (bottom) cf. HN Peg B. Minus and plus errors define the 68.27% confidence interval, determined from 10,000 samples. In cases where >20% of input parameter samples fall outside of the Baraffe et al. (2003) models, lower limits are within 84.13% confidence.
[c] Adopted values are averages from cf. Gl 570D and cf. HN Peg B, except for 2M1043 and SDSS0423.
[d] Assuming no detection of Li in the optical spectrum in Cruz et al. (2007). Owing to poor fit calibration for this object, we adopt instead $T_{\rm eff}$ calculated by applying the Liu et al. (2010) bolometric correction to 2MASS H-band magnitude, typical brown dwarf radius 0.90 ± 0.15R$_{\rm J}$, and conservative mass estimate 70 ± 10 $M_{\rm J}$. We do not adopt a value for log g and instead use the adopted mass and radius to calculate $\langle\rho\rangle$ in Figure 4.
[e] Parameter fits are based on the unresolved spectrum of the binary system and are thus highly suspect. We adopt instead $T_{\rm eff}$ calculated from bolometric magnitude in Vrba et al. (2004), typical brown dwarf radius 0.90 ± 0.15$R_{\rm J}$, and conservative mass estimate 70 ± 10 $M_{\rm J}$. We do not adopt a value for log g and instead use the adopted mass and radius to calculate $\langle\rho\rangle$ in Figure 4.

assumption of emission at the fundamental electron cyclotron frequency.

To best inform our comparison of our results to dynamo models, we also estimate the relevant physical parameters for our brown dwarfs, as discussed in Section 6.2.

6.2. Estimating Physical Parameters of Brown Dwarfs

Effective temperatures ($T_{\rm eff}$) and surface gravities (log g) were estimated for our sample following an updated version of the method described in Burgasser et al. (2006a). We used low-resolution near-infrared spectra from (a) the SpeX Prism Library (Burgasser 2014); (b) data from Burgasser et al. (2004, 2008), Cruz et al. (2004), Liebert & Burgasser (2007), and Siegler et al. (2007); and (c) the indices H_2O–J and K/H defined in Burgasser et al. (2006a, 2006b), which are orthogonally sensitive to temperature and surface gravity variations in T dwarf near-infrared spectra. The indices were measured on solar-metallicity BTSettl08 spectral models (Allard et al. 2011) spanning $T_{\rm eff}$ = 600–1300 K and log g = 3.5–5.5 dex (cgs units). To calibrate these indices, we used the spectra of two brown dwarf companions with broadband model-fit parameters: Gliese 570D (T7.5; Burgasser et al. 2000a), for which Geballe et al. (2001) determine $T_{\rm eff}$ = 804 ± 20 K and log g = 5.14 ± 0.14 dex, and HN Peg B (T2.5; Luhman et al. 2007), for which Leggett et al. (2008) determine $T_{\rm eff}$ = 1115 K and log g = 4.81 dex. Scaling the corresponding model indices to be in agreement with these sources, we then identified the locus of model parameters for which these indices agree with the measured values for our six sources to within 3σ.

Results are shown in Table 4, which compares values from each of the calibrators separately. For 2M1047, SIMP0136, 2M1237, and SDSS1254 we adopt the mean parameters from both Gliese 570D and HN Peg B calibrations. Note that values for 2M1237 are in agreement with those reported in Liebert & Burgasser (2007), while we find a slightly cooler $T_{\rm eff}$ for SDSS1254 and a log g on the low end of values reported by Cushing et al. (2008). The uncertainties for 2M1043 are fairly large and are most likely due to substantial differences between

source and calibrator spectral types (a suitable late L dwarf calibrator was not available). Finally, while we report results for SDSS0423, these are highly suspect given the binary nature of this source (Burgasser et al. 2005). Reported parameter uncertainties reflect uncertainties in the parameters selected to represent the calibrators Gliese 570D and HN Peg B and define the lower and upper bounds of the range relative to the central value that account for 68.27% of the set.

The high surface gravities inferred for 2M1047 and 2M1237 indicate old ages and relatively high (substellar) masses. These were estimated from evolutionary models of Baraffe et al. (2003) by drawing 10,000 $T_{\rm eff}$–log g pairs from each distribution to determine the mean and standard deviations. In both cases, >50% of input parameter samples fall outside of the Baraffe et al. (2003) models and may result in significantly skewed mean values, so we give lower limits within 84.13% confidence. For these sources we infer ages of >2.5 and >3.4 Gyr and masses of >0.026 and >0.028 $M_{\odot}$ within 84.13% confidence, respectively. In contrast, SDSS1254 is matched to a very young age (∼500 Myr) and low mass (∼0.017 $M_{\odot}$). Note that Cushing et al. (2008) report disagreement in log g values based on evolutionary models ($\log g = 4.7$–4.9) and spectral model fits ($\log g = 5.0$–5.5), which these authors speculate may be due to unresolved multiplicity. Our difficulties in inferring the properties of 2M1043 may be related to this source's unusual cloud properties, as it is one of the reddest L8 dwarfs known ($J - K_{\rm s} = 1.97 \pm 0.08$). Its reported optical spectrum shows no indication of Li I absorption (Cruz et al. 2007), implying a mass of ∼0.011 $M_{\odot}$ and age of ∼600 Myr, although this feature may have been masked by poor continuum detection.

For objects whose parameters are not well constrained by the above method, we follow Vrba et al. (2004) and adopt a typical radius of $0.90 \pm 0.15\ R_{\rm J}$ from the Burgasser (2001) study of radius distribution in Burrows et al. (1997) L and T dwarf evolutionary models. We adopt a typical late L mass range of $70 \pm 10\ M_{\rm J}$. For 2M1043, we apply a bolometric correction calculated for spectral type L8 using the polynomial fit from Liu et al. (2010) to the 2MASS H-band magnitude. Using $M_{\odot,\rm bol} = 4.7554 \pm 0.0004$ mag and $L_{\odot,\rm bol}$[4] $= (3.827 \pm 0.0014) \times 10^{33}$ erg s^{-1}, we convert the bolometric magnitude to an effective temperature $T_{\rm eff} = 1390 \pm 180$ K. For SDSS0423, we adopt $T_{\rm eff} = 1678^{+174}_{-137}$ K as derived by Vrba et al. (2004). We include these parameters in Table 4.

6.3. A Simple Formalism for Comparing Magnetic Field Measurements

6.3.1. Magnetic Field Topology

Radio observations of highly circularly polarized pulsed emission yield precise measurements of local magnetic field strengths in the magnetospheres of our objects. However, translating them to a global field strength useful for evaluating dynamo models requires topological information that is difficult to determine from radio observations alone.

Lynch et al. (2015) attempted to constrain the field topologies for two pulsing radio dwarfs by modeling their radio dynamic spectra, inferring localized loops and loss-cone ECM from their modeling. In contrast, Kuznetsov et al. (2012) similarly model the radio pulses of one of the dwarfs examined by Lynch et al. (2015) and found that a highly inclined dipole model with active longitudes for shell-type electron distributions reproduces the pulses with greater fidelity than a loss-cone distribution. Others have inferred dipole-dominated (Yu et al. 2011), quadrupole-dominated (Berger et al. 2009), or small-scale-dominated (Cook et al. 2014; Williams et al. 2014) field geometries for pulsing radio dwarfs. Similar extrapolations have been made for Jovian radio emission using ExPRES (Exoplanetary and Planetary Radio Emissions Simulator) by Hess et al. (2008, 2011). However, the latter use a plethora of additional information to help constrain their calculation, including information on the radio source distribution, the beaming in the planetary environment, a planetary magnetic field model, and precise knowledge of the planetary inclination to the line of sight, none of which are currently available for the dynamic spectra of ultracool dwarfs. We do not attempt to recover the field topologies of our objects here.

Instead, we consider the case where a dipole drives the observed emission. Although direct confirmation of the electrodynamic engine(s) at work in our objects is required to infer whether our magnetic field measurements are indeed of the dipole component or are instead from higher-order components, we note that detailed observations of the magnetized solar system planets show that the dipole component is most likely to produce auroral emission. Specifically, interactions between the large-scale planetary magnetic field with the solar wind (Isbell et al. 1984), the planetary field with orbiting moons such as the Jupiter-Io current system (Goldreich & Lynden-Bell 1969), and corotation breakdown of a plasma sheet in the planetary magnetosphere drive the electrodynamic engines of the solar system planets (Cowley & Bunce 2001; Hill 2001; Bagenal et al. 2014; Badman et al. 2015, and references therein). In all cases, energy is coupled into the upper atmosphere from distances sufficient for the planetary dipole components to dominate.

For our objects, M–I coupling via corotation breakdown and satellite interaction have been proposed as likely drivers (Schrijver et al. 2011; Nichols et al. 2012; Hallinan et al. 2015). We first consider satellite interaction. For a brown dwarf with a rocky satellite, the Roche limit occurs at ∼3.7R_* (Murray & Dermott 1999). Even at this minimum distance, dipole fields dominate over higher-order fields that are a factor of 3 stronger at the surface. In comparison, corotation breakdown occurs at 30–50$R_{\rm J}$ for Jupiter (Cowley & Bunce 2001; Hill 2001; Vogt et al. 2011, and references therein) and at 3–4$R_{\rm S}$ for Saturn (Stallard et al. 2010). In these cases, dipole fields of surface field strengths ∼2–50 times weaker than a quadrupole surface field would dominate at the corotation breakdown radius.

ZDI by Morin et al. (2010, hereafter JM10) suggests that objects significantly below the fully convective boundary with ∼kilogauss large-scale fields are dipole dominated, with the majority of their magnetic energy lying in the dipole component. Specifically, they find that magnetic topologies of 11 M5–M8 dwarfs fall into either a strong or weak large-scale field regime (strong LSF and weak LSF, respectively). In the strong LSF regime, the large-scale field is of order kilogauss with 66%–90% of the reconstructed magnetic energy in the dipole component and is temporally stable over at least ∼3 yr, the length of the study. In the weak LSF regime, multipolar field topologies with much weaker ∼0.1 kG large-

[4] Adopted from Eric Mamajek's Star Notes: https://sites.google.com/site/mamajeksstarnotes/basic-astronomical-data-for-the-Sun.

scale fields vary significantly on yearly timescales. If the results of Morin et al. (2010) apply to late L and T dwarfs, then objects in the strong LSF regime are unlikely to host quadrupolar fields a factor of three or more times stronger than the dipole component, and the dipole field would drive the M–I coupling currents.

In contrast, Williams et al. (2014) argue that weak LSF objects may be X-ray dim/radio bright (departing from the Güdel–Benz relation) instead of X-ray bright/radio dim (more aligned to the Güdel–Benz relation). They suggest that objects in the weak LSF regime likely experience less magnetic activity than objects in the strong LSF regime, hypothesizing that the decreased magnetic activity in weak LSF objects results in correspondingly underluminous X-ray emission, but that small-scale reconnection events can provide a source of radio-emitting electrons. However, we note that in the standard reconnection model of chromospheric heating, X-ray and radio luminosities are tightly correlated (Güdel & Benz 1993; Güdel 2002; Benz & Güdel 2010; Forbrich et al. 2011, and references therein), except for extremely small solar flares, which are in fact comparatively radio underluminous rather than X-ray dim/radio bright. Accordingly, the presence of small-scale reconnection events from a strong small-scale field (as in the weak LSF regime) would result in objects that adhere more closely to the Güdel–Benz relation.

Instead, the lowering of fractional ionization can explain the relative decrease in X-ray luminosities (Mohanty et al. 2002). This does not necessarily impact the radio emission, which is produced above the photosphere or chromosphere irrespective of the mechanism by which it is produced and does not necessarily have the same dependence on fractional ionization as coronal heating. It is also important to note that previous Zeeman broadening studies for 9 of the 11 stars studied in JM10 measured mean surface field magnitudes of order kilogauss (Reiners & Basri 2007; Reiners et al. 2009), regardless of which field regime the star occupied. This implied that the small-scale fields rather than the large-scale ones are quite strong in the weak-field regime. However, in such a scenario, we note that even though the current understanding of M–I coupling does not require the fields to be dipolar, they must be large-scale and strong (kilogauss or stronger to fit observations), precluding the possibility that even strong small-scale fields could drive the M–I coupling.

In the case that JM10 does not extend to our objects, late L and T dwarfs may in fact be more analogous to gas giant planets than to M dwarfs. Jupiter and Saturn are both dipole dominated, with the quadrupole and octupole moments at ∼20% of the dipole moment in Jupiter (Acuna & Ness 1976), and the quadrupole moment in Saturn only ∼7% of its dipole moment (Russell 1993). Despite significant higher-order moments present in the Jovian field, the auroral radio emission produced by Jupiter is thought to be dominated by the dipolar field component (Hill 2001).

While it is possible for higher-order components to drive M–I coupling currents, it is clear that the dipole field can efficiently generate auroral currents. Therefore, we treat the dipole case and will revisit alternatives when additional information on the magnetic fields of ultracool dwarfs becomes apparent.

6.3.2. Relating Magnetic Fields Measured from Auroral Radio Emission to Zeeman Techniques

Under the assumption that auroral emission can be associated with the dipole component of the magnetic field, we now relate our magnetic field measurements to those obtained from Zeeman broadening and ZDI observations so that we may compare our ECM measurements to the C09 results, which use Zeeman-based measurements. To begin, it is important to understand what information each technique yields and its limitations, and we refer the reader to more detailed discussion in Reiners (2012) and Morin (2012) and the references therein.

Zeeman broadening measurements from spectral observations of magnetically sensitive lines provide mean surface field magnitudes B_s, averaged over the photospheric surface of stars, or in rare cases, averaged over the magnetically active regions of the star. For stars where the Zeeman splitting of the σ components can be resolved, both the mean magnetic field magnitude B_s and filling factor f may be measured from the magnitude of the splitting and the relative depths of the σ and π components, respectively (Valenti et al. 1995; Johns-Krull & Valenti 1996, 2000). This requires atomic lines to be relatively isolated for comparison with continuum flux. M5 or later-type objects suffer from spectra increasingly contaminated by molecular lines, and lines become dominated by pressure broadening. In cases where the Zeeman splitting cannot be resolved from the intrinsic line width, the filling factor remains entangled with the mean field, and it is possible to measure only $B_s = B_Z f$. Reiners & Basri (2007) were able to measure mean field magnitudes by comparing the FeH features of 24 M2–M9 stars to reference spectra with known $B_Z f$, with ∼15%–30% uncertainties (Shulyak et al. 2010; Reiners 2012). The method described by Reiners & Basri (2006) is limited by the reference spectra; $B_Z f$ is measured in reference to a zero-field spectrum and a 3.9 kG spectrum, so only fields less than 3.9 kG can be quantified, though it is unlikely that the object serving as the zero-field reference is in fact magnetically inactive. Finally, Zeeman broadening techniques have yet to be successfully applied to objects beyond M9, where rotational broadening blends useful molecular lines. Despite limitations, Zeeman broadening provides a straightforward and convenient framework within which to interpret measurements when testing dynamo predictions.

ZDI provides approximate reconstructions of surface field topologies, allowing estimates of the magnetic energy in different field components (for example, the dipole). However, as applied with existing instruments, ZDI measurements are only sensitive to larger-scale fields, especially in very dim and fast rotators such as our objects. The sensitivity of ZDI is limited by current abilities to adequately resolve polarized flux. Inadequate resolution can lead to the apparent canceling out of observational signatures of opposite-polarity fluxes and mask magnetic fields at smaller spatial scales. For this reason, ZDI is more sensitive to large-scale field structures that can be fully resolved by existing instruments (Reiners & Basri 2009; Yadav et al. 2015), and JM10 have found that the dipole energy can vary by ∼10%–30%, with significant confusion between the dipole and quadrupole components. Additionally, instruments used to map the magnetic fields of cool stars were limited to two of the four Stokes parameters (I, V) until very recently (Rosén et al. 2015), which further limits the sensitivity of ZDI in fully capturing magnetic field topologies. Finally, ZDI maps

can vary widely depending on the particular entropy weighting prescription used when phase coverage is insufficient. Nonetheless, the sensitivity of ZDI to large-scale fields has provided vital insight into large-scale fields. Field topologies of stars appear to change from being dominated by a weak nonaxisymmetric toroidal field to a strong axisymmetric poloidal field as they cross into the fully convective regime (Donati et al. 2008; Morin et al. 2008), and JM10 found evidence for bistable field topologies in late M dwarfs, as discussed in Section 6.3.1.

Using either of the Zeeman techniques to measure magnetic fields is currently impossible for objects beyond spectral type M9, yet the mass regime occupied by L and T dwarfs is critical for probing the efficacy of any fully convective dynamo model. Radio observations of ECM emission provide a new window for probing magnetic activity in a mass regime where Zeeman broadening techniques cannot currently reach. Because the measured magnetic field magnitudes are dependent only on the frequency of the emission cutoff, measurements from radio observations are not subject to the same sources of uncertainty that affect the accuracy of Zeeman broadening measurements. However, ECM measurements also have limitations. Rather than measuring an average field strength, radio observations give a single measurement with great accuracy of the local magnetic field strength in the region of the magnetosphere corresponding to the emission. Additionally, they are likely primarily sensitive to large-scale fields, and the data in isolation are not sufficient for reconstructing the field topology. Finally, without observing emission cutoffs, we are limited to interpreting our measurements as lower bounds to global maximum surface field strengths.

To estimate the lowest possible bound on the global rms surface field strength of an object from a single local radio-derived measurement, we consider an idealized dipole case, which we will adjust as additional topological information becomes available. Our interest in obtaining a conservative lower limit allows us to assume the following simplifications for all of our objects:

1. The magnetic field is perfectly dipolar (the presence of higher-order fields will positively contribute to the rms surface field).
2. The lower-bound field strength measured from our ECM observations, $B_{\rm ECM}$, is the field strength at the magnetic pole at the photosphere. In reality, the emission likely samples the field at a location that does not correspond exactly with the magnetic pole. Moreover, until we observe a frequency cutoff, the emission corresponds to a location in the magnetosphere that is a nonzero altitude above the photosphere, so the actual surface polar field strength can only be equal or greater in all cases.
3. Brown dwarfs are perfect spheres.

We calculate the mean surface dipole field, beginning with the expression for a dipole field,

$$\boldsymbol{B}(\boldsymbol{r}) = \frac{\mu_0}{4\pi}\left[\frac{3\hat{n}\left(\hat{n}\cdot\boldsymbol{m}\right)-\boldsymbol{m}}{|\boldsymbol{r}|^3}\right], \quad (1)$$

where $\hat{n} = \boldsymbol{r}/|\boldsymbol{r}|$ is the unit vector in the direction to the point on the sphere for which the field strength is calculated and $\boldsymbol{m}$ is the magnetic dipole moment. Averaging over the surface of the star shows that the mean squared surface field strength due to the dipole field is

$$\langle B_{\rm s,dip}^2\rangle = \frac{1}{2}B_{\rm ECM}^2. \quad (2)$$

In the case where our objects have purely dipolar fields, $\langle B_{\rm s,dip}\rangle^{1/2}$ would be equivalent to the mean surface field magnitude $B_{\rm s} = B_{Zf}$ as measured by Zeeman broadening, with a filling factor of 100%. Where our objects do not have purely dipolar fields, we consider two cases. If higher-order fields are anti-aligned with the dipole field, such that they contribute negatively to the magnetic flux at the pole, then $\langle B_{\rm s,dip}\rangle^{1/2}$ as calculated above will underestimate the lower bound of the mean surface field magnitude. If higher-order fields are aligned with the dipole such that they contribute positively to the flux at the magnetic pole, then the field strength measured from radio emission will overestimate the rms surface dipole field.

To understand the severity of such a possible overestimation, we return to the Morin et al. (2010) study. While Morin et al. (2011a, 2011b) interpret the result as possible evidence for a dynamo bistability, Kitchatinov et al. (2014) have also proposed that it is evidence of an M-dwarf magnetic cycle. No objects have been observed to be in a transition between the strong-field and weak-field regimes, suggesting that if such a transition occurs, as in a magnetic cycle, the transition is very fast and is unlikely to impact the interpretation of our field measurements. We know from the observed ECM emission and our discussion in Section 6.3.1 that our objects likely occupy the strong LSF regime of a possible bistable dynamo or magnetic cycle. This implies relatively weak higher-order fields, limiting any overestimation of the mean surface field magnitude.

6.4. An Application to Dynamo Models: Comparison to Christensen 2009 Model

We now attempt to test the scaling law presented by C09. C09 showed that for planets and fully convective and rapidly rotating ($P < 4$ days) stars, the convected energy flux available may generate the magnetic field strength. In a departure from prevailing dynamo scaling laws, the central tenet to their model was an energy balance between kinetic and magnetic energies and ohmic dissipation and convective heat transport, rather than a force balance between the Coriolis, Lorentz, buoyancy, and pressure forces (Christensen & Aubert 2006). Surprisingly, they found that the magnetic field strength is independent of both magnetic diffusivity and rotation rate and instead depends strongly only on the buoyancy flux and dynamo size. In particular, they show that for Jupiter, Earth, and a sample of stars including T Tauri stars, old M dwarfs, and main sequence stars with $P < 4$ days, the following relation is empirically consistent:

$$\langle B^2\rangle/\left(2\mu_0\right) = cf_{\rm ohm}\langle\rho\rangle^{1/3}\left(Fq_0\right)^{2/3}. \quad (3)$$

Here $\langle B^2\rangle$ is the squared magnetic field averaged over the whole volume of the dynamo region rather than the surface of the star. $f_{\rm ohm}$ is the ratio of ohmic dissipation to total dissipation and is nominally assumed to be $f_{\rm ohm} \approx 1$. F is a volume average of the temperature scale height divided by the length scale of the largest convective structures, and for their purposes, C09 assume $F = 1$ and 1.19 for stars and Jupiter, respectively. For the purposes of our analysis, we adopt $F = 1$. Parameter q_0 is the bolometric flux at the outer boundary of the

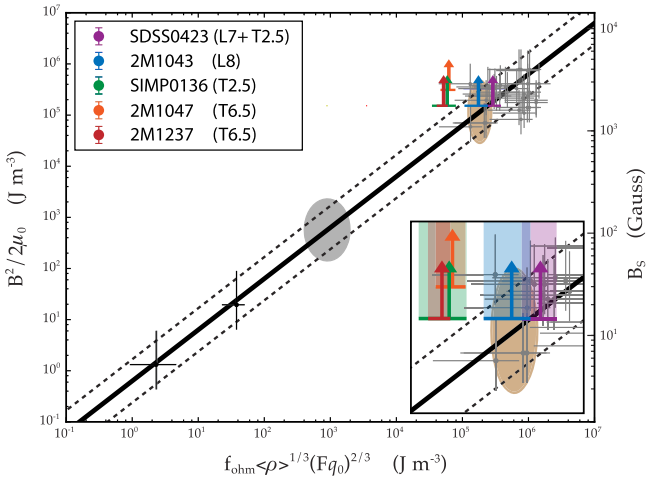

Figure 4. Reproduction of Figure 2 from C09, showing their proposed dynamo scaling relation with 3σ uncertainties for fully convective, rapidly rotating objects (black solid line and dashed lines, respectively). Gray points represent T Tauri stars and old M dwarfs. Black points represent Earth and Jupiter. The brown ellipse indicates the predicted position for a 1500 K brown dwarf, and the gray ellipse indicates the predicted position for a 7 M_J exoplanet. Our detected targets are overplotted, with upward-pointing arrows to indicate that our measurements are lower bounds and horizontal bars to indicate estimated uncertainties. The inset shows more clearly our estimated uncertainties. We adopt a minimum surface field strength of 2.5 kG for our newly detected objects. For 2M1047, we adopt 3.6 kG as measured by Williams & Berger (2015).

dynamo regions, which C09 obtain from the effective surface temperatures of the stars. Finally, μ_0 is permeability, $\langle\rho\rangle$ is the mean density of the dynamo region, and c is a proportionality constant. Figure 4 reproduces this scaling law. Significantly, the wide mass range that the above empirical relation describes tantalizingly hints that the scaling law may be generalizable for all convection-driven dynamos.

The C09 model calls for the mean internal field strength $\langle B\rangle$ of dynamo regions, and an ideal test of their model would utilize direct measurements of the magnetic field inside the dynamo itself. However, measuring these data is impossible. Instead, they estimate $\langle B\rangle$ in several ways. The most direct observational tests available to C09 are Zeeman broadening measurements from spectral observations of Ti I lines in T Tauri stars by Johns-Krull (2007) and K and M stars by Saar et al. (1996) and FeH lines in M dwarfs by Reiners & Basri (2007). C09 additionally adapt ZDI data of mid-M dwarfs by Morin et al. (2008).

The lower-bound mean surface field magnitude $B_{s,dip}$ that we calculated for our objects allows us to very straightforwardly compare our field measurements with those predicted by C09. We treat $B_{s,dip}$ for each object as a lower-bound Zeeman broadening measurement B_s and convert it to $\langle B\rangle$ by following C09 and multiplying by a factor of $\langle B\rangle/B_s \approx 3.5$, which they report is the typical ratio found in their geodynamo simulations. In a recent study of 2M1047, Williams & Berger (2015) detected a pulse at ~10 GHz, corresponding to a lower-bound surface field strength of 3.6 kG for this object. We adopt this value in our comparison to field strengths predicted by C09.

We overlay our most conservative field constraints from auroral radio emission on our reproduction of the C09 scaling law in Figure 4. All of our T dwarfs depart mildly from the C09 scaling relation, suggesting four possibilities: (1) parameters beyond convective flux and dynamo size may influence magnetic fields in brown dwarfs, (2) brown dwarfs have a systematically larger value for the parameter converting external field to internal field, (3) their fields are systematically stronger at the poles than what a dipole predicts, or (4) their field topologies are not dominated by dipoles. These possibilities would not necessarily undermine the basic premises of the proposed scaling law but simply add more uncertainty to the precision with which it can be applied.

It is important to remember that dynamo scaling laws are powerful tools for elucidating which general physical characteristics and behaviors matter, but they describe an inherently chaotic process, and the laws are not deterministic. It is possible that C09 may in fact be largely conceptually correct in the scaling law that they propose, but the parameters on which their law depends may differ from group to group. For instance, the dynamo region extends over ~6–10 orders of magnitude in density in low-mass stars (Saumon et al. 1995). The outermost part of the dynamo action is in a region that is much less dense than the mean density of the dynamo region, yet that could well be the region that determines the observed field because it is closest to the outer boundary. Another possibility is that the appropriate density to use may be defined differently between brown dwarfs and low-mass stars. Additionally, parameters such as $\langle B\rangle/B_s$ depend on boundary conditions, rotation rate, density structure, specific properties of the outer insulating shell (present in Jupiter and brown dwarfs, but not in low-mass stars), etc. Finally, the C09 model is specific to dipole-dominated fields (>35% of field strength in the dipole component), so a departure from the relation may indicate field topologies dominated by higher-order fields.

Nevertheless, it is notable that some of our objects have lower-bound field strengths that are systematically higher than what C09 predict when using parameter definitions that they adopted. The dynamo surface in Jupiter is at ~0.85R_J (Guillot et al. 2004), whereas it is near the surface of M dwarfs. For our objects, the dynamo surface may be more interior than in M dwarfs, causing the adopted values of q_0, $\langle\rho\rangle$, and B_s to increase. However, B^2 rises faster than $\langle\rho\rangle^{1/3}(q_0)^{2/3}$ as a function of internal radius, independent of field topologies, so our T dwarfs may in fact depart more dramatically. Pushing subsequent studies to higher frequencies to observe emission cutoffs will be necessary for obtaining the best possible constraints on field measurements derived from auroral radio emission.

6.5. Implications of Auroral Radio Emission Correlated with Brown Dwarf Weather and Hα Emission

Prior to our work, radio surveys of ~60 L6 or later objects yielded only one detection (Antonova et al. 2013; Route & Wolszczan 2013), resulting in a detection rate of just ~1.4%. In contrast, we have achieved a notably higher detection rate of four of five objects, not including the previously detected 2M1047, by departing from previous target selection strategies and biasing our targets for previously confirmed Hα emission, or in the case of SIMP0136, optical/IR variability. Several of our objects also exhibited tentative IR variability. Selection effects from inclination angles or increased instrument sensitivity may contribute to our dramatically higher success rate, but it is also clear that biasing our sample for optical auroral emission provides a good means to finding radio-emitting brown dwarfs.

While the relationship between IR variability and auroral radio emission remains uncertain, our results are intriguing when viewed in the context of brown dwarf weather. *J*-band variability appears to be common in L and T dwarfs (Enoch et al. 2003; Clarke et al. 2008; Buenzli et al. 2014; Radigan 2014; Radigan et al. 2014; Metchev et al. 2015). Included in our target sample is the canonical dust-variable T dwarf SIMP0136, which exhibits large-amplitude (>5%) IR variability. Also included were tentatively low-amplitude variable objects SDSS0423, 2M1237, and SDSS1254. Clouds in brown dwarf atmospheres have been proposed to interpret observed photometric and spectroscopic variability, and where objects have been observed at multiple wavelengths, some proposed models rely on patchy clouds of variable thicknesses and temperatures (Marley et al. 2010; Apai et al. 2013; Burgasser et al. 2014) to explain wavelength-dependent variability. Our results point to the possibility that an additional variability mechanism may be at play, as postulated by Hallinan et al. (2015).

The success of our selection strategy is especially compelling in light of simultaneous radio and optical spectroscopic observations of the M8.5 dwarf LSR J1835+3259 (hereafter LSR J1835) by Hallinan et al. (2015), whose results in fact motivated our selection strategy. Their study shows features in the radio dynamic spectrum and in the optical spectrum that vary in either phase or anti-phase with each other, with a 2.84 hr period that corresponds to the known rotation period of LSR J1835. Hallinan et al. (2015) assert that auroral current systems can explain the Balmer line emission and observed multiwavelength periodicity. Specifically, they argue that the downward-spiraling population of electrons that gives rise to the observed ECM emission also causes collisional excitation of the neutral hydrogen in the atmosphere upon impact, with subsequent de-excitation via line emission powering the observed Balmer emission. Additionally, the electron current supplies the brown dwarf atmosphere with excess free electrons, possibly contributing to increased H^- opacity in the auroral feature. The increased H^- opacity would cause the upper atmosphere of the auroral feature to become optically thick, appearing lower in temperature than the photosphere. Such an auroral H^- "cloud" could explain the phased and anti-phased light curves at various wavelengths observed in both LSR J1835 and TVLM 513–46546 (Littlefair et al. 2008), another M8.5 brown dwarf known to emit both quiescent and periodically pulsing radio emission, as well as Hα, with a lasting ~0.4-period offset between the optical emission and the radio pulses (Hallinan et al. 2007; Berger et al. 2008; Wolszczan & Route 2014; Lynch et al. 2015).

Our results corroborate the unified auroral model proposed by Hallinan et al. (2015) for even the coolest dwarfs. In late L and T dwarfs such as our targets, molecular hydrogen dominates the atomic hydrogen in the atmosphere, and observed photometric variability may in part be explained by localized heating of the atmosphere within the auroral feature by the precipitating electron beam. Morley et al. (2014) showed that heating of the atmosphere at different depths perturbs the pressure versus temperature profile and can indeed cause spectral variability. Regardless of where in the atmosphere heating occurs, the highest amplitude variability occurs in absorption features redward of ~2.2 μm, which could lead to variability in the *K* and *L* bands. Encouragingly, K_s-band variability has been observed in SIMP0136, as well as tentatively for SDSS0423, and Metchev et al. (2015) report that 36^{+26}_{-17}% of T dwarfs vary by $\geqslant$0.4% at 3–5 μm. However, the incidence rate for dust variability is much higher than for auroral emission (Kirkpatrick et al. 2000, 2008; Burgasser et al. 2003; Cruz et al. 2007; Buenzli et al. 2014; Radigan 2014; Radigan et al. 2014; Heinze et al. 2015; Metchev et al. 2015; Pineda et al. submitted to ApJ), suggesting that auroral emission may only play a role in some cases, such as the highly variable SIMP0136. Finally, we note that even in the absence of atomic hydrogen, Hα emission can still occur. The incoming populations of free electrons and protons can recombine to excited states, or the molecular hydrogen may dissociate to excited atomic hydrogen, subsequently de-exciting via Balmer emission.

In addition to the possible correlation with IR variability, all previous detections of pulsed radio emission from ultracool dwarfs have been accompanied by detectable levels of quiescent radio emission, with no reported detections of pulsed emission in isolation. Although the properties of the quiescent emission are consistent with incoherent synchrotron or gyrosynchrotron emission, the physical processes governing the pulsed and quiescent emission are likely causally related, with the possibility of a shared electrodynamic engine powering the emission.

To better understand the relationship between Hα, radio, and IR variability, additional simultaneous multiwavelength observations and detailed models investigating atmospheric heating from the auroral currents are needed.

7. CONCLUSIONS

We detected five of six late L/T dwarfs in the 4–8 GHz band, including first detections for four objects, quintupling the number of radio-detected objects later than spectral type L6. For four of our objects, including previously detected 2M1047, we observe highly circularly polarized pulsed emission. We also tentatively observe circularly polarized pulsed emission from a fifth object, 2M1237. All of our objects with pulsed emission also exhibit quiescent emission, as is the case for all previously detected radio brown dwarfs. This suggests that pulsed and quiescent phenomena are almost certainly related, though the mechanism for quiescent emission is still unclear.

Biasing our sample for Hα emission or optical/IR variability provides a good means to finding these objects, implying that the Hα emission may be the optical counterpart of auroral activity observed in the radio. We additionally note that several of our objects are either confirmed or tentative IR-variable sources, including the well-known dust-variable T dwarf SIMP0136. Viewed in light of recent studies by Hallinan et al. (2015) and Morley et al. (2014), our radio detections hint that auroral activity may also be related to brown dwarf weather in some cases.

Our data confirm kilogauss magnetic fields down to spectral type T6.5, demonstrating the efficacy of ECM as a tool for probing the magnetic fields of the coolest dwarfs in a mass gap that is critical for informing fully convective dynamo models.

We develop a framework for comparing magnetic field measurements derived from ECM emission with measurements derived from Zeeman broadening and ZDI techniques. Using our framework, we provide strong constraints for rms surface field strengths in late L/T dwarfs and demonstrate that our T dwarfs have magnetic fields that may be inconsistent with the

C09 model. This suggests that parameters beyond convective flux may influence magnetic field generation in brown dwarfs.

M.M.K. thanks Jackie Villadsen, E. Sterl Phinney, Ulrich Christensen, and Shri Kulkarni for illuminating and helpful conversations.

This publication makes use of data products from the Two Micron All Sky Survey, which is a joint project of the University of Massachusetts and the Infrared Processing and Analysis Center/California Institute of Technology, funded by the National Aeronautics and Space Administration and the National Science Foundation.

The National Radio Astronomy Observatory is a facility of the National Science Foundation operated under cooperative agreement by Associated Universities, Inc.

J.S.P. was supported by a grant from the National Science Foundation Graduate Research Fellowship under grant no. DGE-1144469.

REFERENCES

Acuna, M. H., & Ness, N. F. 1976, JGR, 81, 2917
Allard, F., Homeier, D., & Freytag, B. 2011, in ASP Conf. Ser. 448, 16th Cambridge Workshop on Cool Stars, Stellar Systems, and the Sun, ed. C. Johns-Krull, M. K. Browning, & A. A. West (San Francisco, CA: ASP), 91
Antonova, A., Doyle, J. G., Hallinan, G., Golden, A., & Koen, C. 2007, A&A, 472, 257
Antonova, A., Hallinan, G., Doyle, J. G., et al. 2013, A&A, 549, A131
Apai, D., Radigan, J., Buenzli, E., et al. 2013, ApJ, 768, 121
Artigau, É, Bouchard, S., Doyon, R., & Lafrenière, D. 2009, ApJ, 701, 1534
Artigau, É, Doyon, R., Lafrenière, D., et al. 2006, ApJL, 651, L57
Artigau, E., Nadeau, D., & Doyon, R. 2003, in IAU Symp. 211, Brown Dwarfs, ed. E. Martín (Cambridge: Cambridge Univ. Press), 451
Badman, S. V., Branduardi-Raymont, G., Galand, M., et al. 2015, SSRv, 187, 99
Bagenal, F., Adriani, A., Allegrini, F., et al. 2014, SSRv, 1
Baraffe, I., Chabrier, G., Barman, T. S., Allard, F., & Hauschildt, P. H. 2003, A&A, 402, 701
Basri, G. 2001, in ASP Conf Ser. 223, 11th Cambridge Workshop on Cool Stars, Stellar Systems and the Sun, ed. R. J. Garcia Lopez, R. Rebolo, & M. R. Zapaterio Osorio (San Francisco, CA: ASP), 261
Benz, A. O., & Güdel, M. 2010, ARA&A, 48, 241
Berger, E. 2002, ApJ, 572, 503
Berger, E. 2006, ApJ, 648, 629
Berger, E., Ball, S., Becker, K. M., et al. 2001, Natur, 410, 338
Berger, E., Basri, G., Fleming, T. A., et al. 2010, ApJ, 709, 332
Berger, E., Basri, G., Gizis, J. E., et al. 2008, ApJ, 676, 1307
Berger, E., Rutledge, R. E., Phan-Bao, N., et al. 2009, ApJ, 695, 310
Browning, M. K. 2008, ApJ, 676, 1262
Buenzli, E., Apai, D., Radigan, J., Reid, I. N., & Flateau, D. 2014, ApJ, 782, 77
Burgasser, A. J. 2001, PhD thesis, California Institute of Technology
Burgasser, A. J. 2007, ApJ, 659, 655
Burgasser, A. J. 2014, in Astronomical Society of India Conf. Ser. 11, International Workshop on Stellar Spectral Libraries, ed. H. P. Singh, P. Prugniel, & I. Vauglin (Bangalore: BASI), 7
Burgasser, A. J., Burrows, A., & Kirkpatrick, J. D. 2006a, ApJ, 639, 1095
Burgasser, A. J., Geballe, T. R., Leggett, S. K., Kirkpatrick, J. D., & Golimowski, D. A. 2006b, ApJ, 637, 1067
Burgasser, A. J., Gillon, M., Faherty, J. K., et al. 2014, ApJ, 785, 48
Burgasser, A. J., Gillon, M., Melis, C., et al. 2015a, AJ, 149, 104
Burgasser, A. J., Kirkpatrick, J. D., Brown, M. E., et al. 1999, ApJL, 522, L65
Burgasser, A. J., Kirkpatrick, J. D., Brown, M. E., et al. 2002a, ApJ, 564, 421
Burgasser, A. J., Kirkpatrick, J. D., Cutri, R. M., et al. 2000a, ApJL, 531, L57
Burgasser, A. J., Kirkpatrick, J. D., Liebert, J., & Burrows, A. 2003, ApJ, 594, 510
Burgasser, A. J., Kirkpatrick, J. D., Reid, I. N., et al. 2000b, AJ, 120, 473
Burgasser, A. J., Liebert, J., Kirkpatrick, J. D., & Gizis, J. E. 2002b, AJ, 123, 2744
Burgasser, A. J., Liu, M. C., Ireland, M. J., Cruz, K. L., & Dupuy, T. J. 2008, ApJ, 681, 579
Burgasser, A. J., McElwain, M. W., Kirkpatrick, J. D., et al. 2004, AJ, 127, 2856
Burgasser, A. J., Melis, C., Todd, J., et al. 2015b, AJ, 150, 180
Burgasser, A. J., Melis, C., Zauderer, B. A., & Berger, E. 2013, ApJL, 762, L3
Burgasser, A. J., & Putman, M. E. 2005, ApJ, 626, 486
Burgasser, A. J., Reid, I. N., Leggett, S. K., et al. 2005, ApJL, 634, L177
Burrows, A., Marley, M., Hubbard, W. B., et al. 1997, ApJ, 491, 856
Carson, J. C., Marengo, M., Patten, B. M., et al. 2011, ApJ, 743, 141
Chabrier, G., & Baraffe, I. 1997, A&A, 327, 1039
Chabrier, G., & Küker, M. 2006, A&A, 446, 1027
Christensen, U. R., & Aubert, J. 2006, GeoJI, 166, 97
Christensen, U. R., Holzwarth, V., & Reiners, A. 2009, Natur, 457, 167
Clarke, F. J., Hodgkin, S. T., Oppenheimer, B. R., Robertson, J., & Haubois, X. 2008, MNRAS, 386, 2009
Cook, B. A., Williams, P. K. G., & Berger, E. 2014, ApJ, 785, 10
Cowley, S. W. H., & Bunce, E. J. 2001, P&SS, 49, 1067
Cruz, K. L., Burgasser, A. J., Reid, I. N., & Liebert, J. 2004, ApJL, 604, L61
Cruz, K. L., Reid, I. N., Kirkpatrick, J. D., et al. 2007, AJ, 133, 439
Cruz, K. L., Reid, I. N., Liebert, J., Kirkpatrick, J. D., & Lowrance, P. J. 2003, AJ, 126, 2421
Cushing, M. C., Marley, M. S., Saumon, D., et al. 2008, ApJ, 678, 1372
Delfosse, X., Forveille, T., Martín, E. L., et al. 2001, A&A, 366, L13
Delfosse, X., Forveille, T., Perrier, C., & Mayor, M. 1998, A&A, 331, 581
Dobler, W., Stix, M., & Brandenburg, A. 2006, ApJ, 638, 336
Donati, J.-F., Forveille, T., Collier Cameron, A., et al. 2006, Sci, 311, 633
Donati, J.-F., Morin, J., Petit, P., et al. 2008, MNRAS, 390, 545
Drake, S. A., Simon, T., & Linsky, J. L. 1989, ApJS, 71, 905
Enoch, M. L., Brown, M. E., & Burgasser, A. J. 2003, AJ, 126, 1006
Forbrich, J., Wolk, S. J., Güdel, M., et al. 2011, in ASP Conf. Ser. 448, 16th Cambridge Workshop on Cool Stars, Stellar Systems, and the Sun, ed. C. Johns-Krull, M. K. Browning, & A. A. West (San Francisco, CA: ASP), 455
Fuhrmeister, B., & Schmitt, J. H. M. M. 2004, A&A, 420, 1079
Gastine, T., Morin, J., Duarte, L., et al. 2013, A&A, 549, L5
Geballe, T. R., Knapp, G. R., Leggett, S. K., et al. 2002, ApJ, 564, 466
Geballe, T. R., Saumon, D., Leggett, S. K., et al. 2001, ApJ, 556, 373
Girardin, F., Artigau, É, & Doyon, R. 2013, ApJ, 767, 61
Gizis, J. E., Monet, D. G., Reid, I. N., et al. 2000, AJ, 120, 1085
Goldman, B., Cushing, M. C., Marley, M. S., et al. 2008, A&A, 487, 277
Goldreich, P., & Lynden-Bell, D. 1969, ApJ, 156, 59
Güdel, M. 2002, ARA&A, 40, 217
Güdel, M., & Benz, A. O. 1993, ApJL, 405, L63
Guillot, T., Stevenson, D. J., Hubbard, W. B., & Saumon, D. 2004, in The Interior of Jupiter, ed. F. Bagenal, T. E. Dowling, & W. B. McKinnon (Cambridge: Cambridge Univ. Press), 35
Hall, P. B. 2002, ApJL, 580, L77
Hallinan, G., Antonova, A., Doyle, J. G., et al. 2006, ApJ, 653, 690
Hallinan, G., Antonova, A., Doyle, J. G., et al. 2008, ApJ, 684, 644
Hallinan, G., Bourke, S., Lane, C., et al. 2007, ApJL, 663, L25
Hallinan, G., Littlefair, S. P., Cotter, G., et al. 2015, Natur, 523, 568
Harding, L. K., Hallinan, G., Boyle, R. P., et al. 2013, ApJ, 779, 101
Heinze, A. N., Metchev, S., & Kellogg, K. 2015, ApJ, 801, 104
Hess, S., Cecconi, B., & Zarka, P. 2008, GeoRL, 35, 13107
Hess, S. L. G., Bonfond, B., Zarka, P., & Grodent, D. 2011, JGRA, 116, 5217
Hill, T. W. 1979, JGR, 84, 6554
Hill, T. W. 2001, JGR, 106, 8101
Isbell, J., Dessler, A. J., & Waite, J. H., Jr. 1984, JGR, 89, 10716
Johns-Krull, C. M. 2007, ApJ, 664, 975
Johns-Krull, C. M., & Valenti, J. A. 1996, ApJL, 459, L95
Johns-Krull, C. M., & Valenti, J. A. 2000, in ASP Conf. Ser. 198, Stellar Clusters and Associations: Convection, Rotation, and Dynamos, ed. R. Pallavicini, G. Micela, & S. Sciortino (San Francisco, CA: ASP), 371
Kirkpatrick, J. D., Cruz, K. L., Barman, T. S., et al. 2008, ApJ, 689, 1295
Kirkpatrick, J. D., Reid, I. N., Liebert, J., et al. 2000, AJ, 120, 447
Kitchatinov, L. L., Moss, D., & Sokoloff, D. 2014, MNRAS, 442, L1
Koen, C., Matsunaga, N., & Menzies, J. 2004, MNRAS, 354, 466
Kuznetsov, A. A., Doyle, J. G., Yu, S., et al. 2012, ApJ, 746, 99
Lane, C., Hallinan, G., Zavala, R. T., et al. 2007, ApJL, 668, L163
Leggett, S. K., Geballe, T. R., Fan, X., et al. 2000, ApJL, 536, L35
Leggett, S. K., Saumon, D., Albert, L., et al. 2008, ApJ, 682, 1256
Liebert, J., & Burgasser, A. J. 2007, ApJ, 655, 522
Littlefair, S. P., Dhillon, V. S., Marsh, T. R., et al. 2008, MNRAS, 391, L88
Liu, M. C., Dupuy, T. J., & Leggett, S. K. 2010, ApJ, 722, 311
Luhman, K. L., Patten, B. M., Marengo, M., et al. 2007, ApJ, 654, 570
Lynch, C., Mutel, R. L., & Güdel, M. 2015, ApJ, 802, 106
Marley, M. S., Saumon, D., & Goldblatt, C. 2010, ApJL, 723, L117

McLean, M., Berger, E., & Reiners, A. 2012, ApJ, 746, 23
Metchev, S. A., Heinze, A., Apai, D., et al. 2015, ApJ, 799, 154
Mohanty, S., & Basri, G. 2003, ApJ, 583, 451
Mohanty, S., Basri, G., Shu, F., Allard, F., & Chabrier, G. 2002, ApJ, 571, 469
Morin, J. 2012, in EAS Publications Ser. 57, Evry Schatzman School on Stellar Physics XX III ed. C. Reylé, C. Charbonnel, & M. Schultheis, 165
Morin, J., Delfosse, X., Donati, J.-F., et al. 2011a, in SF2A-2011: Proc. Annual Meeting of the French Society of Astronomy and Astrophysics, Evidence for Dynamo Bistability among Very Low Mass Stars, ed. G. Alecian, K. Belkacem, R. Samadi, & D. Valls-Gabaud, 503
Morin, J., Donati, J.-F., Petit, P., et al. 2008, MNRAS, 390, 567
Morin, J., Donati, J.-F., Petit, P., et al. 2010, MNRAS, 2269
Morin, J., Dormy, E., Schrinner, M., & Donati, J.-F. 2011b, MNRAS, 418, L133
Morley, C. V., Marley, M. S., Fortney, J. J., & Lupu, R. 2014, ApJL, 789, L14
Murray, C. D., & Dermott, S. F. 1999, Solar System Dynamics (Cambridge: Cambridge Univ. Press)
Nichols, J. D., Burleigh, M. R., Casewell, S. L., et al. 2012, ApJ, 760, 59
Pallavicini, R., Golub, L., Rosner, R., et al. 1981, ApJ, 248, 279
Parker, E. N. 1975, ApJ, 198, 205
Phan-Bao, N., Osten, R. A., Lim, J., Martín, E. L., & Ho, P. T. P. 2007, ApJ, 658, 553
Pineda, J. S., Hallinan, G., Kirkpatrick, J. D., et al. 2015, ApJ, submitted
Pizzolato, N., Maggio, A., Micela, G., Sciortino, S., & Ventura, P. 2003, A&A, 397, 147
Radigan, J. 2014, ApJ, 797, 120
Radigan, J., Lafrenière, D., Jayawardhana, R., & Artigau, E. 2014, ApJ, 793, 75
Reid, I. N., Cruz, K. L., Burgasser, A. J., & Liu, M. C. 2008, AJ, 135, 580
Reid, I. N., Kirkpatrick, J. D., Liebert, J., et al. 2002, AJ, 124, 519
Reiners, A. 2012, LRSP, 9, 1
Reiners, A., & Basri, G. 2006, ApJ, 644, 497
Reiners, A., & Basri, G. 2007, ApJ, 656, 1121
Reiners, A., & Basri, G. 2008, ApJ, 684, 1390
Reiners, A., & Basri, G. 2009, A&A, 496, 787
Reiners, A., & Basri, G. 2010, ApJ, 710, 924
Reiners, A., Basri, G., & Browning, M. 2009, ApJ, 692, 538
Rosén, L., Kochukhov, O., & Wade, G. A. 2015, arXiv:1504.00176
Route, M., & Wolszczan, A. 2012, ApJL, 747, L22
Route, M., & Wolszczan, A. 2013, ApJ, 773, 18
Russell, C. T. 1993, RPPh, 56, 687
Saar, S. H. 1994, in IAU Symp. 154, Infrared Solar Physics, ed. D. M. Rabin, J. T. Jefferies, & C. Lindsey, 437
Saar, S. H. 1996, in Recent Measurements of Stellar Magnetic Fields, ed. Y. Uchida, T. Kosugi, & H. S. Hudson (Netherlands: Springer)
Saumon, D., Chabrier, G., & van Horn, H. M. 1995, ApJS, 99, 713
Schmidt, S. J., Cruz, K. L., Bongiorno, B. J., Liebert, J., & Reid, I. N. 2007, AJ, 133, 2258
Schmidt, S. J., Hawley, S. L., West, A. A., et al. 2015, AJ, 149, 158
Schmidt, S. J., West, A. A., Hawley, S. L., & Pineda, J. S. 2010, AJ, 139, 1808
Schrijver, C. J., Aulanier, G., Title, A. M., Pariat, E., & Delannée, C. 2011, ApJ, 738, 167
Shulyak, D., Reiners, A., Wende, S., et al. 2010, A&A, 523, A37
Siegler, N., Close, L. M., Burgasser, A. J., et al. 2007, AJ, 133, 2320
Skrutskie, M. F., Cutri, R. M., Stiening, R., et al. 2006, AJ, 131, 1163
Soderblom, D. R., Stauffer, J. R., Hudon, J. D., & Jones, B. F. 1993, ApJS, 85, 315
Stallard, T., Melin, H., Cowley, S. W. H., Miller, S., & Lystrup, M. B. 2010, ApJL, 722, L85
Stauffer, J. R., Caillault, J.-P., Gagne, M., Prosser, C. F., & Hartmann, L. W. 1994, ApJS, 91, 625
Tinney, C. G., & Reid, I. N. 1998, MNRAS, 301, 1031
Treumann, R. A. 2006, A&ARv, 13, 229
Valenti, J. A., Marcy, G. W., & Basri, G. 1995, ApJ, 439, 939
Vogt, M. F., Kivelson, M. G., Khurana, K. K., et al. 2011, JGRA, 116, 3220
Vrba, F. J., Henden, A. A., Luginbuhl, C. B., et al. 2004, AJ, 127, 2948
West, A. A., Hawley, S. L., Bochanski, J. J., et al. 2008, AJ, 135, 785
West, A. A., Hawley, S. L., Walkowicz, L. M., et al. 2004, AJ, 128, 426
White, S. M., Kundu, M. R., & Jackson, P. D. 1989, A&A, 225, 112
Williams, P. K. G., & Berger, E. 2015, arXiv:1502.06610
Williams, P. K. G., Berger, E., & Zauderer, B. A. 2013, ApJL, 767, L30
Williams, P. K. G., Cook, B. A., & Berger, E. 2014, ApJ, 785, 9
Winglee, R. M. 1985, JGR, 90, 9663
Wolszczan, A., & Route, M. 2014, ApJ, 788, 23
Yadav, R. K., Christensen, U. R., Morin, J., et al. 2015, ApJL, 813, L31
York, D. G., Adelman, J., Anderson, J. E., Jr., et al. 2000, AJ, 120, 1579
Yu, S., Hallinan, G., Doyle, J. G., et al. 2011, A&A, 525, A39
Zarka, P. 1998, JGR, 103, 20159